

A NEW PERSPECTIVE ON THE JAMMING TRANSITION: REVEALS HIDDEN  
SYMMETRIES

by

PETER MORSE

A DISSERTATION

Presented to the Department of Physics  
and the Graduate School of the University of Oregon  
in partial fulfillment of the requirements  
for the degree of  
Doctor of Philosophy

June 2016

DISSERTATION APPROVAL PAGE

Student: Peter Morse

Title: A New Perspective on the Jamming Transition: Geometry Reveals Hidden Symmetries

This dissertation has been accepted and approved in partial fulfillment of the requirements for the Doctor of Philosophy degree in the Department of Physics by:

Richard Taylor	Chair
Eric Corwin	Advisor
John Toner	Core Member
Marina Guenza	Institutional Representative

and

Scott L. Pratt	Vice President for Research & Innovation/ Dean of the Graduate School
----------------	--

Original approval signatures are on file with the University of Oregon Graduate School.

Degree awarded June 2016

© 2016 Peter Morse

This work is licensed under a Creative Commons

**Attribution-NonCommercial-NoDerivs (United States) License.**



## DISSERTATION ABSTRACT

Peter Morse

Doctor of Philosophy

Department of Physics

June 2016

Title: A New Perspective on the Jamming Transition: Geometry Reveals Hidden Symmetries

Jamming is a physical process which is both easy to describe and incredibly difficult to understand. One such difficulty is that mechanical treatments of jamming focus on pressure, force, stress, and strain, which are identically zero below jamming, making it hard to differentiate systems which are near or far from the transition. Instead, I introduce a geometric framework based on the Voronoi tessellation which treats all of phase space on an equal footing. This work will show that the jamming transition can be seen entirely through the geometry of the local environment of particles encoded in the Voronoi tessellation, and it will build the framework for an as yet undefined field theory for jamming.

This dissertation includes previously published and unpublished coauthored material.

## CURRICULUM VITAE

NAME OF AUTHOR: Peter Morse

### GRADUATE AND UNDERGRADUATE SCHOOLS ATTENDED:

University of Oregon, Eugene, OR  
University of Washington, Seattle, WA

### DEGREES AWARDED:

Doctor of Philosophy, Physics, 2016, University of Oregon  
Master of Science, Physics, 2010, University of Oregon  
Bachelor of Science with a minor in Applied Math, Physics, 2008, University of Washington  
Bachelor of Science, Applied and Computational Mathematical Sciences, 2008, University of Washington

### AREAS OF SPECIAL INTEREST:

Soft Condensed Matter, Jamming, Biophysics

### PROFESSIONAL EXPERIENCE:

Research Assistant, University of Oregon, 2010-2016  
Teaching Assistant, University of Oregon 2009-2010, 2015  
NSF GK-12 Fellow, University of Oregon, 2012-2014  
Research Assistant in Physics and Material Science, University of Washington, 2008-2009

### GRANTS, AWARDS AND HONORS:

Martin and Beate Block Award, Aspen Center for Physics, 2015  
Washington Scholar, Washington Student Achievement Council, 2004-2008

### PUBLICATIONS:

P.K. Morse, and E.I. Corwin, "Hidden Symmetries in Jammed Systems" *Journal of Statistical Mechanics: Theory and Experiment* Accepted (2016).  
P.K. Morse, and E.I. Corwin, "Geometric order parameters derived from the Voronoi tessellation show signatures of the jamming transition." *Soft Matter* **12**, 1248-1255 (2016).  
P.K. Morse, and E.I. Corwin, "Geometric Signatures of jamming in the mechanical vacuum." *Phys Rev Letters* **112**, 115701 (2014).

B.C. Scannell, I. Pilgrim, A.M. See, R.D. Montgomery, P.K. Morse, M.S. Fairbanks, C.A. Marlow, H. Linke, I. Farrer, D.A. Ritchie, A.R. Hamilton, A.P. Micolich, L. Eaves, R.P. Taylor, Probing the sensitivity of electron wave interference to disorder-induced scattering in solid-state devices. *Phys Rev B*, **85**, 195319, (2012).

H.C. Lee, O.E. Vilches, Z. Wang, E. Fredrickson, P.K. Morse, R. Roy, B. Dzyubenko, D.H. Cobden, Kr and 4He adsorption on individual suspended single-walled carbon nanotubes, *Journal of Low Temperature Physics*, **169** (2012).

Z. Wang, J. Wei, P.K. Morse, J.G. Dash, O.E. Vilches, D.H. Cobden, Phase transitions of adsorbed atoms on the surface of a Carbon nanotube, *Science*, **327**, 5965, (2010).

## ACKNOWLEDGEMENTS

All of this work has been done with the guidance of my advisor Eric Corwin, who has shaped me into the scientist that I now am. For various insights on my simulations and analysis in addition to creating a cohesive lab, I would like to thank my labmates: Yasin Karim, Alex Trevelyan, Kyle Welch, and Andy Hammond, as well as Ben Strickland who worked loosely on this project for a summer and our undergraduate researcher Mike van der Naald. I would like to thank John Royer at the National Institute for Standards and Technology for proof-reading all of the papers that are included in this work. I would also like to thank my committee for their advice at various points throughout my graduate career. Of these especially, I would like to thank Richard Taylor, whose lab I joined early on. His unique approach to problems and his focus on novel geometry continues to inspire me. Last, and most importantly, the writing and compiling of this work was done while I was recovering from a severe concussion, and so I would like to thank my parents, my doctors, Roger Smith, and Yasin Karim for providing emotional and physical support. This work would have not been possible by any stretch of the imagination without them.

To my beautiful and supportive partner, who I might have met had it not been for this.



TABLE OF CONTENTS

Chapter	Page
I. INTRODUCTION . . . . .	1
II. GEOMETRIC SIGNATURES OF JAMMING IN THE MECHANICAL VACUUM . . . . .	4
Abstract . . . . .	4
Background . . . . .	4
Methods . . . . .	5
The Voronoi Tessellation . . . . .	9
Maximum Inscribed Sphere . . . . .	10
Conclusion . . . . .	13
Acknowledgments . . . . .	14
III. VORONOI GEOMETRY SHOWS THE JAMMING TRANSITION . . . . .	15
Abstract . . . . .	15
Introduction . . . . .	15
Generating a packing . . . . .	16
Geometry of the Voronoi tessellation . . . . .	20
Analysis . . . . .	26
Conclusion . . . . .	29
Acknowledgments . . . . .	29
IV. HIDDEN SYMMETRIES IN JAMMED SYSTEMS . . . . .	30
Abstract . . . . .	30
Background . . . . .	30
Methods . . . . .	32

Chapter	Page
Discussion . . . . .	36
Conclusion . . . . .	41
Acknowledgments . . . . .	41
V. SUPPLEMENTARY MATERIAL FOR CHAPTER 2 . . . . .	42
VI. SUPPLEMENTARY MATERIAL FOR CHAPTER 3 . . . . .	46
VII. CONCLUSION . . . . .	49
REFERENCES CITED . . . . .	54

LIST OF FIGURES

Figure	Page
1. (a) The Additively Weighted Voronoi tessellation for a polydisperse mixture of particles in two dimensions. The particle shown in blue has a set of nearest neighbors shown in red. (b-d) The maximum inscribed sphere (MIS) in a given Voronoi cell below jamming (b), at jamming (c), and above jamming (d). The physical particle is illustrated as a gray circle, the Voronoi cell is shown in black lines, the MIS is shown as a blue dashed circle, and the contacts between the MIS and the Voronoi cell are shown as red stars. . . . .	6
2. (a) The scaled mean number of neighbors as a function of scaled distance to the jamming point. Shown are $d= 2$ (gray), 3 (black), 4 (purple), 5 (blue), 6 (green), 7 (orange), 8 (red). The $k$ values used for collapse are 1, 1, 1.4, 1.4, 1.2, 1, and 0.75 respectively. All packings are created using the infinite temperature quench (IQ) protocol. Inset, Log-log plot of scaled mean number of neighbors as a function of distance to the jamming point for $d \geq 3$ . Packings plotted in the inset are created using the GM protocol from below the jamming transition (solid lines) and above (dashed lines). (b) Scaled mean neighbor number for varied polydispersity in $d = 3$ . The radii of the polydisperse particles are drawn from a log-normal distribution with $\mu = 1$ and $\sigma$ ranging from 0 (red), 0.05 (black) up to 0.2 (light gray) in steps of 0.05. (c) Scaled mean neighbor number for varied power-law potentials. Values of the order of the potential $\alpha$ range from 1.5 (black) to 4 (light gray) with the Hookean potential ( $\alpha = 2$ ) shown in red. . . . .	8
3. (a) Distributions of radii of MIS at $0.5\phi_J$ (light blue), $0.9\phi_J$ (dark blue), $\phi_J$ (purple), $1.1\phi_J$ (dark red), and $1.5\phi_J$ (light red) for $d = 3$ . The packings above and below jamming were made using the IQ protocol, and the jammed packing was made using the GM protocol from above. (b) Semi-log plot of scaled distribution width of MIS as a function of scaled distance to the jamming transition. The color scheme is the same as in Fig. 2a. (c) Log-log plot of scaled distribution width for packings approaching jamming from below with GM protocol. Inset, power-law behavior shows $\Delta R/r$ approaching $\phi^*$ quadratically. (d) Log-log plot of scaled distribution width for packings approaching jamming from above showing a power-law with exponent 1. (e-f) Plot of the scaled number of constraints on the MIS as a function of scaled distance to the jamming point. Packings are created using the GM protocol. Inset, plot of $\phi^*/\phi_J$ as a function of dimension $d$ . . . . .	11
4. Plots of scaled order parameters vs. the scaled packing fraction. Closed circles represent IQ data, x's represent GM data (from below), and triangles represent ES data (from above). Note that on this linear scale the GM and ES data is nearly all clustered right at $\phi_J$ . The parameters shown are (a) mean surface area, $S$ , (b) standard deviation of volume divided by the mean of the volume, $\tilde{V}$ , (c) mean surface to volume ratio $S/V^{(d-1)/d}$ (d) mean aspect ratio, $A$ , and (e) mean aspect ratio angle $\cos\theta$ . We plot data for $d = 2$ (smaller particles light gray, larger particles dark gray, combined black), $d = 3$ (green), $d = 4$ (red), and $d = 5$ (blue). . . . .	17

5. Log-log plots of each scaled order parameter vs. the scaled packing fraction approaching jamming from below (left) and above (right). Closed circles represent IQ data, x's represent GM data (from below), and triangles represent ES data (from above). The parameters shown are (a,f) mean surface area,  $S$ , (b,g) standard deviation of volume divided by the mean of the volume,  $\tilde{V}$ , (c,h) mean surface to volume ratio  $S/V^{(d-1)/d}$  (d,i) mean aspect ratio,  $A$ , and (e,j) mean aspect ratio angle  $\cos\theta$ . We plot data for  $d = 2$  (smaller particles light gray, larger particles dark gray, combined black),  $d = 3$  (green),  $d = 4$  (red), and  $d = 5$  (blue). . . . . 19
6. Illustration of the aspect ratio axes in two Voronoi cells. For each cell, the short axis is shown in green (short dashes) and the long axis is shown in orange (long dashes). The angle  $\theta$  between the two axes is defined to be the acute angle between the short and long axis. The angle  $\alpha$  between two long axes of different cells is also shown. . . . . 21
7. The normalized long axis correlation between Voronoi cells plotted as a function of distance between particles in  $d = 2 - 5$ . Correlations are shifted vertically to show the effect of changing  $\phi$  with a color scheme that fades from purple ( $\phi = 0$ ) to black ( $\phi = \phi_J$ ) to green ( $\phi = 2\phi_J$ ). Gray dashed lines show the line corresponding to completely uncorrelated axes, open circles denote minima and open stars represent secondary maxima. A black line has been drawn over each curve representing the Savitsky-Golay filter. Data obtained using the IQ protocol. . . . . 23
8. The position of the minimum (closed circles) and secondary maximum (open star) of the correlation shown in Figure as a function of distance from the jamming transition. Colors shown represent dimensions 2 (black), 3 (green), 4 (red), and 5 (blue). . . . . 28
9. Diagram showing the maximum inscribed sphere (MIS) inversion. (a) An initial monodisperse packing is shown with particles colored gray, their radical Voronoi cells in black, and the MIS shown as a dashed blue line. (b) The first step of the MIS inversion with the same color scheme. Note that the MIS from (a) is the new particle, the Voronoi cell has changed, and the system is now polydisperse. . . . . 31
10. Convergence of the MIS inversion. a) Log-linear plot of the mean displacement per particle from the previous MIS iteration. Each line represents a system at a different initial packing fraction, with color scale indicating initial packing fraction as shown beneath the plots. The lower dashed line is drawn at  $\phi_J$  and the upper dashed line is drawn at  $\phi^*$ , the lowest packing fraction for which initial packings are fixed points under the MIS inversion. b) Packing fraction at each step of the MIS inversion, using the same color scheme as a. The upper dashed line is drawn here at  $\phi_J$  and the lower dashed line is at  $\phi^*$ , which is flipped from a. . . . . 34
11. The coarse graining procedure pairs each cell in with the unpaired cell that shares the highest surface area. a) The original Voronoi diagram, b) the system after one step of the coarsening procedure, c) the system after two steps of coarsening. Colors denote the membership in cells after two rounds of coarsening. . . . . 35

Figure	Page
12. Asymptotic properties of the MIS inversion. a) Fixed points of the MIS Inversion are represented by their polydispersity and their final packing fraction. Initial packings start at polydispersities of 0 (closed circles), 0.05 (squares), 0.1 (x's), 0.15 (open circles), and 0.2 (triangles). Points that remain fixed through the entire process lie on the dotted lines associated with their starting polydispersity. Initial packing fraction is coded into the color. b) Asymptotic mean number of contacts $\langle Z \rangle$ as a function of initial packing fraction for $d = 3$ (black), and $d = 4$ (green). . . . .	37
13. Under the coarse graining scheme, the behavior of each parameter of the cells reaches a curve of fixed points as a function of packing fraction. On the left, we have plotted the initial parameter (black) and the first 6 coarse grainings (each corresponding to a lighter shade of gray, with the 6th in red) in three dimensions for the mean number of neighbors (a), mean surface area (b), standard deviation over the mean of volume (c) and aspect ratio (d). In each, we scale by subtracting off and dividing by the order parameter at $\phi_J$ in that iteration, such that the jamming point is always at the origin. On the right (e-h), we have plotted only the original (closed circles) and the 6th iteration (open circles) for $d = 3$ (black) and $d = 4$ (green). . . . .	39
14. Coarse grained aspect ratio cross over shows no evidence of finite size effects. We have plotted 3 system sizes in $d = 3$ at the 6th iteration of the coarsening (as done in figure 13h), with system sizes of 4096 (red open circles), 8192 (blue triangles), and 65536 (black closed circles). . . . .	40
15. Scaled mean number of neighbors vs. scaled packing fraction for various packing protocols. Solid lines represent Infinite Quench data and dashed lines represent Geometric Mean search data. The same values for $\phi_J$ , $N_J$ , and $k$ are used for collapse in each dimension. In general it is not required that we use the same parameters, but we have done so to show how strong the agreement is between the methods used to approach jamming. Shown are $d= 3$ (black), 4 (purple), 5 (blue), 6 (green), 7 (orange), 8 (red). . . . .	42
16. Scaled mean number of neighbors vs. scaled packing fraction for various packing protocols. Solid lines represent Infinite Quench data and dashed lines represent a simulated annealing wherein each point represents a dilation from the previous data point followed by an energy relaxation. The same values for $\phi_J$ , $N_J$ , and $k$ are used for collapse in each dimension. In general it is not required that we use the same parameters, but we have done so to show how strong the agreement is between the methods used to approach jamming. Shown are $d= 3$ (black), 4 (purple), 5 (blue), 6 (green), 7 (orange), 8 (red). . . . .	43
17. Scaled mean number of neighbors vs. scaled packing fraction for various neighbor definitions with polydisperse data in $d = 3$ . Solid lines represent Additively Weighted Voronoi, and dashed lines represent Radical Voronoi (also called the Laguerre tessellation). Behavior at the phase transition is robust against neighbor definitions. As in Figure 2b, values of the order of the potential $\alpha$ range from 1.5 (black) to 4 (light gray) with the Hookean potential ( $\alpha = 2$ ) shown in red. . . . .	44

18. Width of the distribution of Maximum Inscribed Spheres calculated from the middle 15% (red) to 85% (black) of the distribution in steps of 10%. A width of 80% is used in the text. Note that each definition corresponds to a slightly different  $\phi^*$ , but that the general trend of  $\phi^*$  with dimension is robust. The packings analyzed are the same as seen in Figure 3b in the paper. The packings above  $\phi_J$  are made using a Geometric Mean search and the packings from below are made via Infinite Quench. . . . . 45
19. Plots of scaled order parameters vs. the scaled packing fraction. Closed circles represent IQ data, x's represent GM data (from below), and triangles represent ES data (from above). Note that on this linear scale the GM and ES data is nearly all clustered right at  $\phi_J$ . The parameters shown are (a) mean surface area,  $S$ , (b) standard deviation of volume divided by the mean of the volume,  $\tilde{V}$ , (c) mean surface to volume ratio  $S/V^{(d-1)/d}$  (d) mean aspect ratio,  $A$ , and (e) mean aspect ratio angle  $\cos\theta$ . We plot data for  $d = 3$  bidisperse spheres (smaller particles light gray, larger particles dark gray, combined black) and  $d = 3$  monodisperse spheres (green). . . . . 47
20. Log-log plots of each scaled order parameter vs. the scaled packing fraction approaching jamming from below (left) and above (right). Closed circles represent IQ data, x's represent GM data (from below), and triangles represent ES data (from above). The parameters shown are (a,f) mean surface area,  $S$ , (b,g) standard deviation of volume divided by the mean of the volume,  $\tilde{V}$ , (c,h) mean surface to volume ratio  $S/V^{(d-1)/d}$  (d,i) mean aspect ratio,  $A$ , and (e,j) mean aspect ratio angle  $\cos\theta$ . We plot data for  $d = 3$  bidisperse spheres (smaller particles light gray, larger particles dark gray, combined black) and  $d = 3$  monodisperse spheres (green). The slopes shown give the power laws for monodisperse spheres for comparison. . . . . 48

## LIST OF TABLES

Table		Page
1.	Table of $\langle N \rangle$ at zero density for dimension $d$ from 1-8. . . . .	10
2.	Scaling laws and critical values for all parameters $\chi$ , such that $\frac{\chi - \chi_J}{\chi_J} \propto \left(\frac{\phi - \phi_J}{\phi_J}\right)^\gamma$ . Critical values quoted have their error in the least significant digit, which is reported in parentheses. Both GM and ES data agree on each critical value. All critical values are unitless except for $S_J$ which is reported as the unitless $S_J N_{\text{particles}}^{(d-1)/d}$ . For $d = 2$ , we report separately on $\chi_J$ values for the larger particles, the smaller particles, and the system as a whole. . . . .	21
3.	Table of values for $\phi^*$ , and $\phi_J$ used in this manuscript. Note that there are a range of values for the jamming transition dependent on method. . . . .	43

## CHAPTER I

### INTRODUCTION

To best enjoy this thesis, go to the beach and grab a handful of sand and hold onto it tightly. The sand holds its shape in your hands. As long as you hold on tight, this sand is a solid: mechanically jammed and acting as a whole. But as soon as you let your grip loose, the sand flows like water between your fingers. This sand, unconstrained, acts like a liquid: unjammed and acting like many weakly interacting particles. With the simple loosening or tightening of your grip, you have witnessed a phase transition that is just as physically real as the transition from ice to water, and yet something seems more simplistic about it. In doing this experiment, you might expect that in the realm of phase transitions this jamming or unjamming transition would be more well understood than the more dramatic ice to water transition. You would be wrong.

There are many unsolved problems in the jamming community. In order to understand and predict behavior in a phase transition, there needs to be a field theory. As it stands, there is no mean field theory in finite dimensions, and furthermore, there are no small parameters that can be expanded upon to create a field theory. There has been a proposed field theory solution in infinite dimensions [1], but there is still much work to be done to translate the results to a three dimensional world. Because there is no field theory in finite dimensions, there is no explanation of power law scaling and no justification for the specific jamming point  $\phi_J$ .

The difficulty in characterizing granular systems is evident from the simplest experiments. While I've used the analogy of flowing sand as a liquid, it is fundamentally different from a liquid like water. If you fill a bathtub with sand, the sand will conform to the shape of the tub like water, but unlike water the sand will hold your weight and you will be able to stand on top of it (unlike the previous experiment, I would like to strongly discourage attempting this one unless you've got a great plumber). This is due to the size and energy scales of sand particles and water molecules being vastly different. The energy of water molecules is almost entirely thermal, whereas the thermal energy is a negligible fraction of a sand particle's total energy. For this reason, I will only be addressing particles which are athermal.

Sand particles are both frictional and non-spherical, and both of these properties present major difficulties. There is some debate on how to treat friction in the context of jamming [2–5],



and so as a starting point I have restricted all of my work to frictionless spheres. In theory, my work could be expanded to include ellipses or polymer chains, both of which would yield new and exciting results due to inherent symmetry breaking. It is my hope that this work will be expanded to someday cover both frictional cases and non-spherical particles, either by myself or by others.

The jamming of frictionless spheres can be split into two classes: thermal hard sphere glasses and athermal soft sphere jamming. Hard spheres are ones that cannot ever overlap, and thus they can only be treated below jamming. There is a great deal of literature on hard spheres, including a spectacular review of modern physics [1]. Soft spheres in this context are not ones that deform, but rather ones that are allowed to overlap. By using soft spheres, we can treat the entirety of phase space above and below jamming equally, and so I have decided to focus entirely on them in this work.

The goal of my work has always been to treat athermal soft sphere systems the same regardless of whether they are below, above, or at the jamming transition. This means that mechanical quantities such as pressure, stress, strain, and force will be useless, because below jamming, these quantities are all identically zero [6]. Instead, I will focus on the local environment encoded into the Voronoi tessellation [7], which splits all of space into regions which are closest to each particle. The Voronoi tessellation is well defined for all packing fractions, and so it treats all systems agnostically. Once I have the tessellation of a given packing, I can then calculate any geometric property of the cells and compare them to different packing fractions and preparation procedures.

This work will show that the jamming transition can be seen entirely through the geometry of the local environment of particles encoded in the Voronoi tessellation, and it will build the framework for an as yet undefined field theory for jamming. Chapter 2 will introduce this concept by showing both the jamming transition and a pre-jamming phase transition in the statistics of the Voronoi tessellation. Chapter 3 will focus on expanding this understanding by including more geometric parameters and by defining a correlation function which shows a signature of the transition. Chapter 4 will introduce two transformations involving the Voronoi tessellation, which will reveal as yet unseen symmetries of the jamming transition. Chapter 2 has been published in Physical Review Letters [8] and chapter 3 has been published in Soft Matter [9]. At the time

of this writing, chapter 4 has been accepted but not yet published in the Journal of Statistical Mechanics: Theory and Experiment.

## CHAPTER II

### GEOMETRIC SIGNATURES OF JAMMING IN THE MECHANICAL VACUUM

#### **Abstract**

Jamming has traditionally been studied as a mechanical phenomenon and characterized with mechanical order parameters. However, this approach is not meaningful in the “mechanical vacuum” of systems below jamming in which all mechanical properties are precisely zero. We find that the network of nearest neighbors and the geometric structure of the Voronoi cell contain well defined and meaningful order parameters for jamming which exist on both sides of the transition. We observe critical exponents in these order parameters and an upper critical dimension of 3. Further, we present evidence for a new incipient-jamming phase below the jamming transition marked by additional symmetry in the Voronoi tessellation.

This work was originally published in Physical Review Letters [8]. Eric Corwin advised all of this work and so he is added as a coauthor, but the majority of the work and writing was my own.

#### **Background**

Since 1727 when the Reverend Stephen Hales studied the contact statistics of peas compressed in a pot [10] the study of jamming has primarily concerned itself with mechanical properties. It is well known how pressure [6], bulk and shear modulus [11–13], stress and strain [6], force [14], and contact number [15, 16] scale with packing fraction  $\phi$  above the jamming point  $\phi_J$  [17]. While these properties can be used as order parameters to study the mechanical jamming transition, this understanding does not extend to the “mechanical vacuum.” The mechanical vacuum describes states below jamming wherein the system has no mechanical response and lacks stable force carrying contacts. This leaves half of the phase space with a trivial order parameter that does not capture the physical reality that a system slightly below jamming is very different from one far below jamming [18]. This phase space has previously been studied within the realm of liquid theory and hard sphere jamming [1, 19–21] but the structural properties of static unjammed packings have yet to be addressed.

High dimensional sphere packings offer an opportunity to study the underlying physics and geometry of jamming [18, 22, 23]. Recent attempts to construct a field theory for jammed systems have been successful in describing mechanical properties. The Gaussian Replica Theory uses a mapping between spin glass systems and jammed systems to develop a field theory with predictive power for some scalings around jamming [1]. This theory is applicable in arbitrary dimensions and correctly predicts  $\phi_J$  will take on a range of values that are method dependent [23]. Recent simulational work has exploited finite size scaling of the mechanical properties of jamming for  $d = 2$  and  $d = 3$  to find critical exponents and evidence for an upper critical dimension of  $d_{UCD} = 2$  [24]. However, because these works are restricted to mechanical properties they can not describe the physics of systems below jamming.

The local structure of jammed systems has also emerged as an active area of study. The properties of the nearest neighbor network for sphere packings at and above jamming are key components of Granocentric models [25–29]. These models are purely local in scope and yet manage to predict global properties, suggesting that the local geometry plays an important role in jamming.

## Methods

In this paper we analyze simulations of sphere packings using two local geometric quantities which are derived from the Additively Weighted Voronoi tessellation [30] of space around each particle: 1) the mean number of nearest neighbors and 2) the maximum inscribed sphere in each cell (Fig. 1). Both are well defined above and below jamming and, as will be shown, contain a signature of the jamming transition.

### *Simulation: Energy minimization*

Packings of particles are created similarly to references [23, 31]. Particles exist in a  $d$ -dimensional hypercube with periodic boundary conditions and unit side length and interact with a contact potential dependent on their dimensionless overlap

$$\delta = 1 - \frac{\|\vec{x}_1 - \vec{x}_2\|}{r_1 + r_2} \quad (2.1)$$

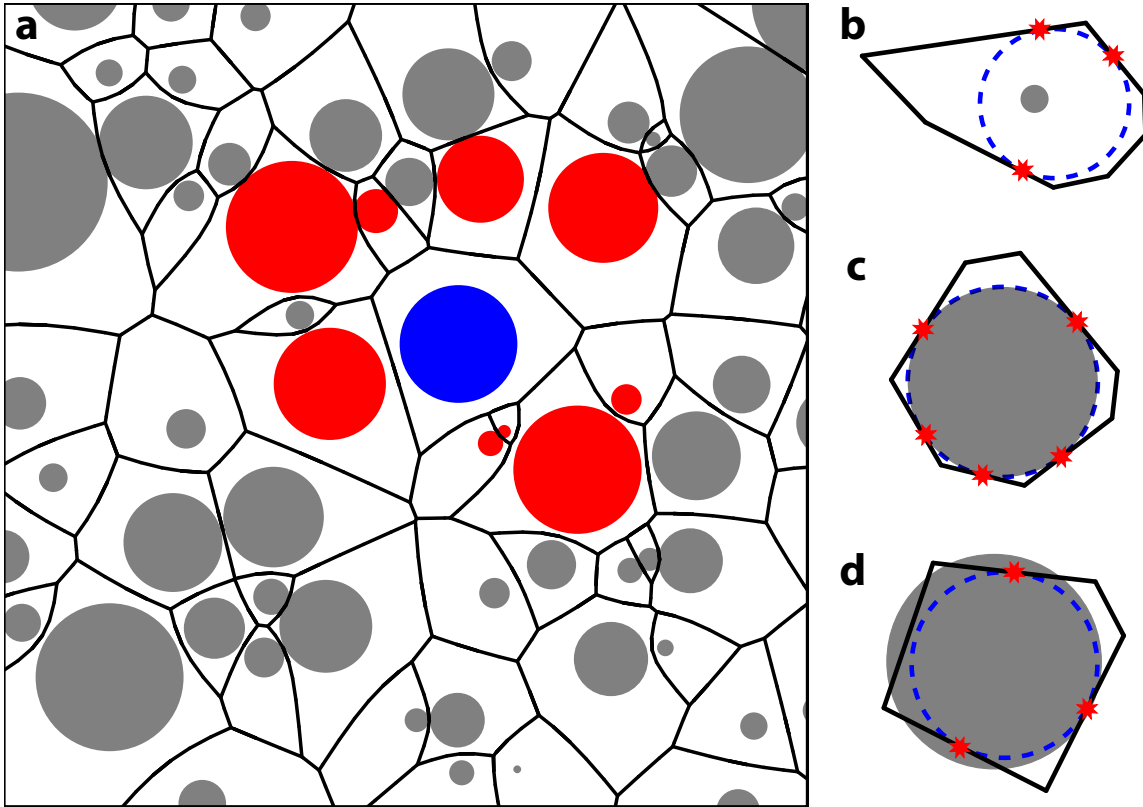


FIGURE 1. (a) The Additively Weighted Voronoi tessellation for a polydisperse mixture of particles in two dimensions. The particle shown in blue has a set of nearest neighbors shown in red. (b-d) The maximum inscribed sphere (MIS) in a given Voronoi cell below jamming (b), at jamming (c), and above jamming (d). The physical particle is illustrated as a gray circle, the Voronoi cell is shown in black lines, the MIS is shown as a blue dashed circle, and the contacts between the MIS and the Voronoi cell are shown as red stars.

where  $\vec{x}_1$  and  $\vec{x}_2$  are the particle positions and  $r_1$  and  $r_2$  are the radii. The potential is defined as

$$V(\delta) = \begin{cases} \frac{\epsilon}{\alpha} \delta^\alpha & : \delta > 0 \\ 0 & : \delta \leq 0 \end{cases} \quad (2.2)$$

where  $\alpha$  is the order of the potential ( $\alpha = 2$  for a Hookean potential and 2.5 for a Hertzian potential) and  $\epsilon$  is the characteristic energy scale chosen to be 1. Unless specified, we use  $\alpha = 2$ . A packing is considered unjammed if the energy of overlap per particle is less than  $10^{-20}$ .

*Simulation: Infinite quench and golden mean search*

We explore a wide range of packing fractions using two protocols: 1) infinite temperature quench (IQ) 2) golden mean search (GM). The IQ protocol is used to create a packing at a specified  $\phi$  by placing particles randomly throughout the simulation volume with appropriately scaled radii [15]. The system is then relaxed to its local energy minimum using a home-built, GPGPU-optimized version of conjugate gradient minimization [32] or the fast inertial relaxation engine (FIRE) [33] running on the University of Oregon's ACISS supercomputer. We demonstrate in Supplemental Figures 1 and 2 that our results close to jamming are robust to choices among our minimization techniques. The GM protocol is used to approach arbitrarily close to the jamming point,  $\phi_J$ . The resulting value of  $\phi_J$  is dependent on whether jamming is approached from below or above, but the properties of packings at the transition do not depend on the packing history [23]. A GM packing is created from above (below) by choosing two packing fractions that bound  $\phi_J$ . An initial packing is created at the bound above (below) using the IQ protocol. The radii of particles in this packing are then scaled by a uniform factor to achieve an intermediate packing fraction and re-minimized. If the resulting packing remains above (below) jamming it is made the new upper (lower) bound and the process continues. If it is below (above) then it becomes the new lower (upper) bound and a new packing is made by dilating the previous upper (lower) bound packing. This process is continued until the upper and lower bounds differ by less than 1 part in  $10^{15}$ .

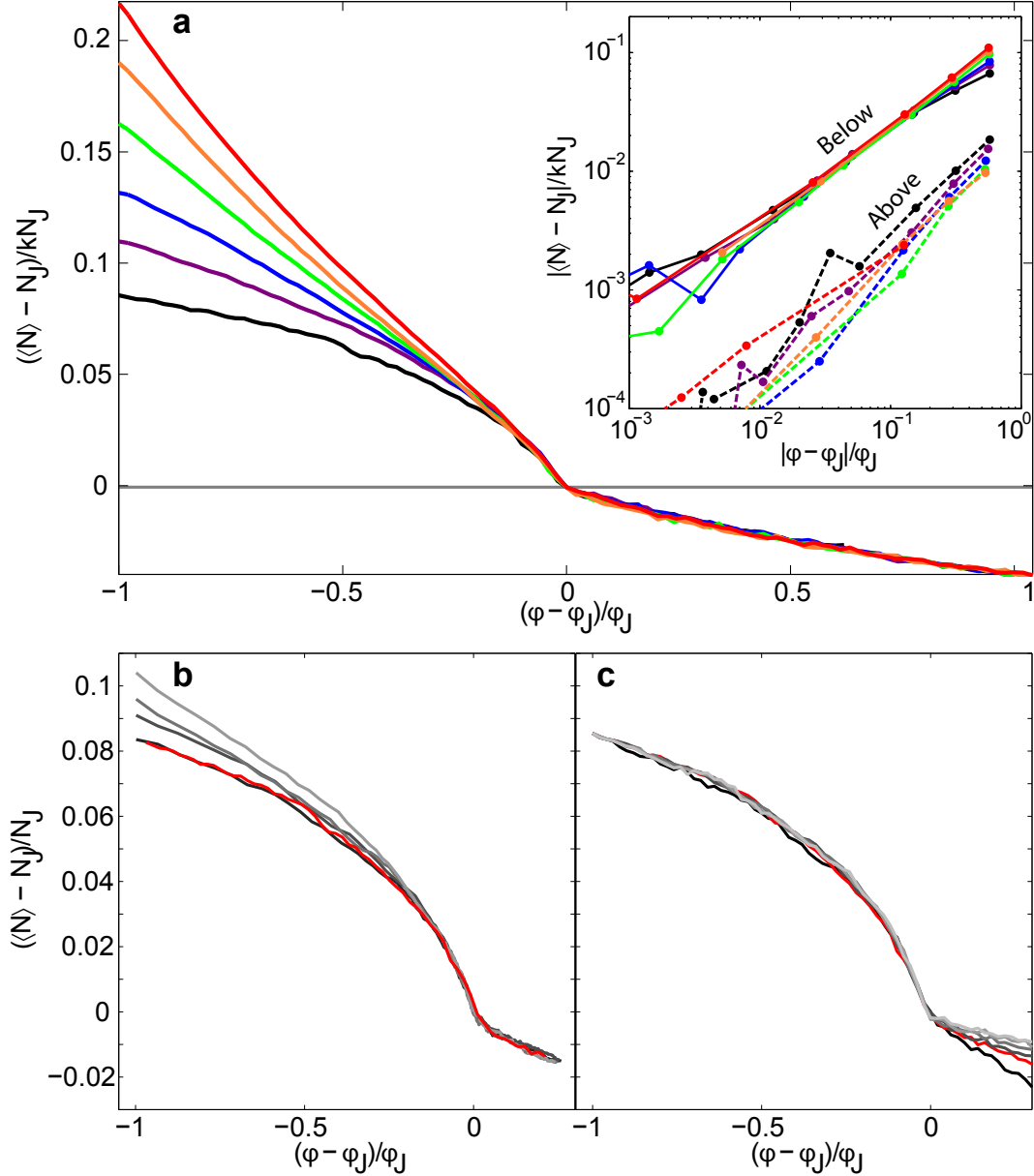


FIGURE 2. (a) The scaled mean number of neighbors as a function of scaled distance to the jamming point. Shown are  $d=2$  (gray), 3 (black), 4 (purple), 5 (blue), 6 (green), 7 (orange), 8 (red). The  $k$  values used for collapse are 1, 1, 1.4, 1.4, 1.2, 1, and 0.75 respectively. All packings are created using the infinite temperature quench (IQ) protocol. Inset, Log-log plot of scaled mean number of neighbors as a function of distance to the jamming point for  $d \geq 3$ . Packings plotted in the inset are created using the GM protocol from below the jamming transition (solid lines) and above (dashed lines). (b) Scaled mean neighbor number for varied polydispersity in  $d = 3$ . The radii of the polydisperse particles are drawn from a log-normal distribution with  $\mu = 1$  and  $\sigma$  ranging from 0 (red), 0.05 (black) up to 0.2 (light gray) in steps of 0.05. (c) Scaled mean neighbor number for varied power-law potentials. Values of the order of the potential  $\alpha$  range from 1.5 (black) to 4 (light gray) with the Hookean potential ( $\alpha = 2$ ) shown in red.

## The Voronoi Tessellation

The nearest neighbor network determines the local environment of a particle. For a given particle, the Additively Weighted Voronoi (sometimes called the navigation map or Johnson-Mehl tessellation) cell contains all points in space closer to the particle’s surface than to that of any other particle [30]. For monodisperse particles this reduces to the Voronoi diagram in which all cells have flat interfaces. Two particles are said to be nearest neighbors if their respective cells share an interface. In order to calculate the Additively Weighted Voronoi tessellation in high dimensions, we implemented the algorithm described by Boissonnat and Delage [? ]. However, we should note that our results continue to hold for other choices of tessellation, most notably the Radical Voronoi (or Laguerre) tessellation, as demonstrated in Supplemental Figure 3. As a packing approaches jamming the neighbor network is very sensitive to the small spatial rearrangements of particles. We observe a continuous phase transition in the mean number of neighbors  $\langle N \rangle$  as a function of packing fraction (Fig. 2a). All curves for dimensions  $d \geq 3$  collapse onto a single master curve near  $\phi_J$  when scaled as  $(\langle N \rangle - N_J)/kN_J$  vs  $(\phi - \phi_J)/\phi_J$ , where  $k$  is a tunable parameter of order 1 and  $N_J$  is the mean number of nearest neighbors at jamming and  $\phi_J$  is the jamming density found through our GM protocol. Note that  $k$  is a scale factor which only depends on dimension, similar to the universal amplitude ratio of the lambda transition [34]. This master curve has power-law scaling on both sides of the transition point with exponents  $\simeq 0.75$  as shown in the inset to Fig. 2a, demonstrating that  $\phi_J$  controls the physics on both sides of the transition. There is no *a priori* reason why the power laws on either side should be the same or different and our data is insufficient to conclusively distinguish the two. For  $d = 2$  this curve is trivially flat due to the Euler relation which requires  $\langle N \rangle = 6$  for all  $\phi$ . Since this collapse only occurs for  $d \geq 3$  we have evidence for an upper critical dimension of  $d_{UCD} = 3$ , in stark contrast to the mechanical picture which yields  $d_{UCD} = 2$  [6, 24].

Individual curves peel away from the master curve in Fig. 2a when sufficiently far below  $\phi_J$ . There is a seemingly trivial point in phase space at  $\phi = 0$  which nonetheless controls the physics of low-density packings. At zero density the contact potential and polydispersity are meaningless as every particle has radius  $r = 0$  and zero overlap. The network of nearest neighbors at this point is thus the result of a Poisson process and its properties are calculable using stochastic geometry [35, 36]. Analytic values for  $\langle N \rangle$  at zero density have been found for



d	1	2	3	4	5	6	7	8
$\langle N \rangle$	2	6	$\frac{48\pi^2}{35} + 2$	$\frac{340}{9}$	89.3(8)	203.(6)	458.(8)	1016.(3)

TABLE 1. Table of  $\langle N \rangle$  at zero density for dimension  $d$  from 1-8.

$d \leq 4$  [36] and agree with our results to within numerical error. Exact values have not yet been derived in higher dimensions but are easily numerically computed with our simulations (Table 1). Systems very close to zero density are controlled by this point up to a cross-over density, beyond which the system is controlled by  $\phi_J$ .

The effect of sample polydispersity is shown in Fig. 2b. Varying polydispersity changes the numerical value of  $\phi_J$  [37], but the shape of the curve near jamming is unchanged. This suggests that the distance between surfaces of particles is more important to the dynamics of the phase transition than center-to-center distance. Thus, monodisperse and polydisperse packings are controlled by the same physics in this regime.

Figure 2c demonstrates the effect of varying the contact potential. We use power law contact potentials (Eqn. 2.2) with order  $\alpha$  ranging from 1.5 to 4. All potentials follow the same master curve below jamming. This is unsurprising because below jamming the only role of the potential is to prevent overlap. Above jamming, the potential determines the distribution of overlaps between particles which in turn determines the local structure of the packing. This is manifested by a change in the slope of the curve above  $\phi_J$  with lower order potentials giving steeper slopes, suggesting that higher order potentials tend to lock in local structure and give higher barriers to structural rearrangements.

### Maximum Inscribed Sphere

The maximum inscribed sphere (MIS) in the Voronoi cell of each particle contains a very different signature of the jamming transition. The radius  $R$  of the MIS in a given Voronoi cell is calculated using an algorithm similar to the FIRE minimization of particle packings and an imposed repulsive harmonic potential between the inscribed sphere and the cell walls. We perform a GM search by choosing two radii that bound the true MIS radius. If the minimized energy is less than  $10^{-20}$ , the test radius is now used as the lower bound, and if it is greater, the test radius is used as the upper bound. The search process is continued until the upper and lower bounds differ by less than 1 part in  $10^{15}$ .

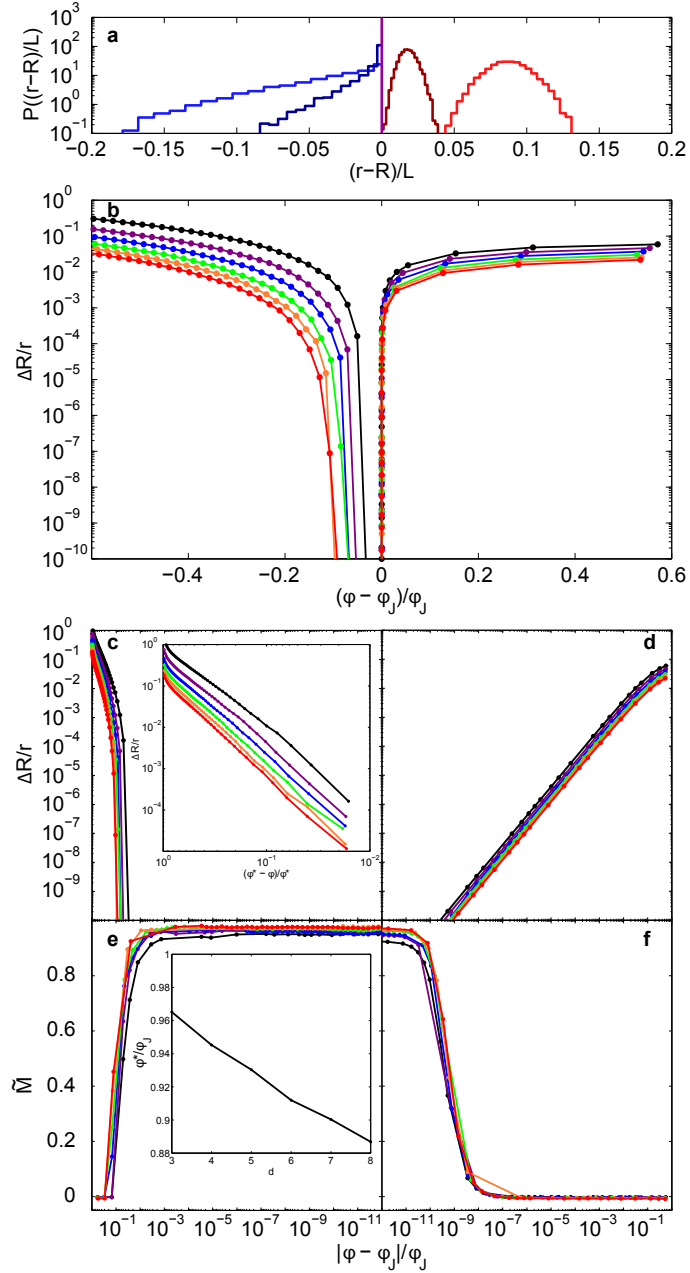


FIGURE 3. (a) Distributions of radii of MIS at  $0.5\phi_J$  (light blue),  $0.9\phi_J$  (dark blue),  $\phi_J$  (purple),  $1.1\phi_J$  (dark red), and  $1.5\phi_J$  (light red) for  $d = 3$ . The packings above and below jamming were made using the IQ protocol, and the jammed packing was made using the GM protocol from above. (b) Semi-log plot of scaled distribution width of MIS as a function of scaled distance to the jamming transition. The color scheme is the same as in Fig. 2a. (c) Log-log plot of scaled distribution width for packings approaching jamming from below with GM protocol. Inset, power-law behavior shows  $\Delta R/r$  approaching  $\phi^*$  quadratically. (d) Log-log plot of scaled distribution width for packings approaching jamming from above showing a power-law with exponent 1. (e-f) Plot of the scaled number of constraints on the MIS as a function of scaled distance to the jamming point. Packings are created using the GM protocol. Inset, plot of  $\phi^*/\phi_J$  as a function of dimension  $d$ .

Figure 3a shows  $P(\frac{r-R}{L})$ , the distribution of the normalized difference between the MIS radii,  $R$ , and the particle radius,  $r$ , for monodisperse particles in  $d = 3$ . We normalize the difference in radii by the characteristic distance between centers  $L = \rho^{-d}$  where  $\rho$  is the number density of particles. Below jamming no particles overlap, therefore the MIS radius  $R$  must be strictly less than the particle radius  $r$  (Fig. 1b). Above jamming every non-rattler particle has some overlap, therefore the MIS radius  $R$  must be strictly greater than the particle radius  $r$  (Fig. 1d). At jamming the particle is fully constrained and kissing the boundaries of the Voronoi cell (Fig. 1c) causing the MIS to be identical to the particle. Therefore, any translation or dilation relative to the jammed particle must puncture the surface of the Voronoi cell. Thus, at jamming  $P(\frac{r-R}{L})$  must be a  $\delta$ -function at zero. In this way jamming links the mechanical structure of a packing to the geometric structure of the nearest neighbor network.

Because the functional form of the MIS distribution changes dramatically, and to discount the influence of rattlers, we characterize its evolution with packing fraction by defining a distribution width  $\Delta R/r$  to be the width of the middle 80% of the distribution. We use this definition of width rather than the standard deviation to minimize the influence of rattlers. We find that our width is robust to changes in this cutoff value (Supplemental Figure 4). When we approach jamming from above (the right side of Fig. 3b) we see a linear convergence to zero in  $\Delta R/r$  at  $\phi_J$  (Fig. 3d). However, when we approach from below jamming (left side of Fig. 3b) we also see a convergence of the width toward zero but at a packing fraction significantly less than  $\phi_J$ . We call this new critical point  $\phi^*$  and find that  $\Delta R/r$  approaches this point from below with a power-law of  $\simeq 2$  (Fig. 3c inset and tabulated in Supplemental Figure 5).

As a consequence of the identity between the particle and the MIS at jamming the mean number of constraints  $\langle M \rangle$  on the MIS should also contain a signature of jamming. In general, the MIS in a convex polytope in  $d$  dimensions is constrained to contact  $M = d + 1$  sides of the cell. However, since jammed packings at  $\phi_J$  are mechanically stable they satisfy isostaticity, which requires the mean number of contacts  $\langle Z \rangle = 2d$  [24]. This in turn requires that the mean number of constraints on the MIS be  $M = 2d$ . In order for an inscribed sphere to have more than  $d + 1$  contacts there must be degeneracy in the constraints. This implies that a heretofore unobserved symmetry must be present in the Voronoi cells at jamming.

We define the normalized number of constraints  $\widetilde{M}$  on an MIS as

$$\widetilde{M} = \frac{M - (d + 1)}{2d - (d + 1)} \quad (2.3)$$

such that at jamming where  $M = 2d$ ,  $\widetilde{M} = 1$  and generically when  $M = d + 1$ ,  $\widetilde{M} = 0$ . As expected, we see a transition in  $\widetilde{M}$  from  $\widetilde{M} = 0$  far from jamming to  $\widetilde{M} = 1$  close to jamming. When approaching jamming from above the transition happens at a distance to  $\phi_J$  comparable to our numerical precision (Fig 3f) whereas when approaching from below the transition occurs at  $\phi^*$  rather than at  $\phi_J$  (Fig. 3e). This is further evidence that  $\phi^*$  is a meaningful critical point related to this new symmetry. The ratio  $\phi^*/\phi_J$  decreases linearly with increasing dimension, indicating that the phase between  $\phi^*$  and  $\phi_J$  becomes more important in higher dimensions (Fig. 3e inset).

### Conclusion

Our results demonstrate that the geometric structure of a packing contains a clear signature of the jamming transition. We have measured critical exponents in order parameters derived from this geometric structure which should prove instrumental to developing a fully realized field theory for both sides of the jamming transition. Surprisingly, we find  $d_{\text{UCD}} = 3$  whereas measures of mechanical properties yield  $d_{\text{UCD}} = 2$ . This result can be interpreted in alternative ways: 1) There are two independent phase transitions, one mechanical and the other geometric, that happen to coincide at precisely the same point in phase space. 2) The jamming/un-jamming transition is a new type of phase transition consisting of linked mechanical and geometric transition with different  $d_{\text{UCD}}$ . Each interpretation is unsettling in its own way. It beggars belief that two entirely independent phase transitions would just happen to precisely coincide so (1) seems quite unlikely. Interpretation (2) requires the extraordinary claim that the jamming transition is characteristically unlike any other understood physical process. Indeed, jamming and by extension the glass transition [38] has been curiously resistant to theoretical explanation. Under either interpretation these results point the way towards new physics.

Finally, we observe a new critical point  $\phi^*$  well below  $\phi_J$ . This new critical point is obscured by the mechanical vacuum, and there is no signature of it in simple statistics of the neighbor network. One can only find it by looking at the local structure of Voronoi cells. It remains to be uncovered what underlying symmetry is revealed by this phase transition.

### **Acknowledgments**

We thank John Toner for helpful discussions. We thank the NSF for support under Career Award DMR-1255370 and NSF GK12 DGE-0742540. The ACISS supercomputer is supported under a Major Research Instrumentation grant, Office of Cyber Infrastructure, OCI-0960354.

## CHAPTER III

### VORONOI GEOMETRY SHOWS THE JAMMING TRANSITION

#### **Abstract**

A jammed packing of frictionless spheres at zero temperature is perfectly specified by the network of contact forces from which mechanical properties can be derived. However, we can alternatively consider a packing as a geometric structure, characterized by a Voronoi tessellation which encodes the local environment around each particle. We find that this local environment characterizes systems both above and below jamming and changes markedly at the transition. A variety of order parameters derived from this tessellation carry signatures of the jamming transition, complete with scaling exponents. Furthermore, we define a real space geometric correlation function which also displays a signature of jamming. Taken together, these results demonstrate the validity and usefulness of a purely geometric approach to jamming.

This work was originally published in *Soft Matter* [9]. Eric Corwin advised all of this work, and so he is added as a coauthor, but the majority of the work and writing was my own.

#### **Introduction**

Over the past two decades the jamming of athermal frictionless spheres has been seen as the limiting case of several different kinds of systems [1, 15, 38–41]. Athermal soft sphere systems can be brought to the limit of zero internal energy and isostaticity, achieving a critically jammed system which is typically characterized by mechanical properties [6, 11, 13, 15, 17, 40]. However, when such systems are below the jamming density there is no longer a mechanical network of force-bearing contacts and so mechanical order parameters are all identically zero. Conversely, hard sphere thermal liquids are studied below the glass or jamming transition and are characterized by dynamic quantities such as mobility and pressure [1, 41, 42]. As density is increased they reach the limit of diverging reduced pressure and become a critically jammed system. Above this density, hard sphere systems can not exist. While both athermal soft sphere systems and thermal hard sphere glass systems have been successful models for predicting and measuring scaling exponents of various parameters near the jamming phase transition [1, 13, 15, 41], neither of these model systems speak to the behavior of unjammed athermal

systems. This leaves a gap in the understanding of the athermal jamming transition. In this paper we introduce new geometric order parameters which characterize the athermal jamming transition both above and below jamming, placing both sides of the transition on equal footing and providing a meaningful way to interrogate soft sphere systems below the jamming transition.

The structure of jammed systems has long been studied in terms of geometry [25, 26, 35, 43–46] however a systematic study of geometric changes as a function of distance to the transition has not yet been performed. The Voronoi tessellation [7], which is well defined at all packing fractions, provides a natural lens through which to study both unjammed and overjammed systems. In previous work we have demonstrated that the number of facets (corresponding to the number of nearest neighbors) provides a good order parameter for the jamming transition [8]. This order parameter raised a new problem, however, because it exhibited an upper critical dimension (above which, all order parameters share the same scaling laws) of  $d = 3$ . This stood in contrast to the well known fact that mechanical order parameters exhibit an upper critical dimension of  $d = 2$  [15, 24]. This, coupled with the recent success of replica theory in predicting high finite dimensional scaling [41] has motivated us to explore a range of geometric order parameters in dimensions ranging from  $d = 2$  to  $d = 5$ .

In this paper we show that most geometric properties of the Voronoi tessellation are controlled by the jamming point  $\phi_J$ , suggesting that jamming can be described in purely geometric terms. Further, we present a new geometrically defined correlation function which changes qualitatively at the jamming transition. Surprisingly, none of these measures show any indication of the previously discovered pre-jamming transition, associated with the maximum inscribed sphere of the Voronoi cell, which we have found to happen at a density  $\phi^* < \phi_J$  [8].

### Generating a packing

We simulate packings of frictionless athermal particles with a harmonic contact potential in periodic boundary conditions as described in references [8, 23]. In  $d = 3 - 5$ , we use monodisperse spheres, and in two dimensional systems, we use a 50:50 mixture of bidisperse disks with a ratio of radii that is 1:1.4, known to show mechanical jamming. We present data obtained with three packing protocols: Infinite Quench (IQ)[15], Geometric Mean (GM)[8, 23], and Energy Sweep (ES)[41].

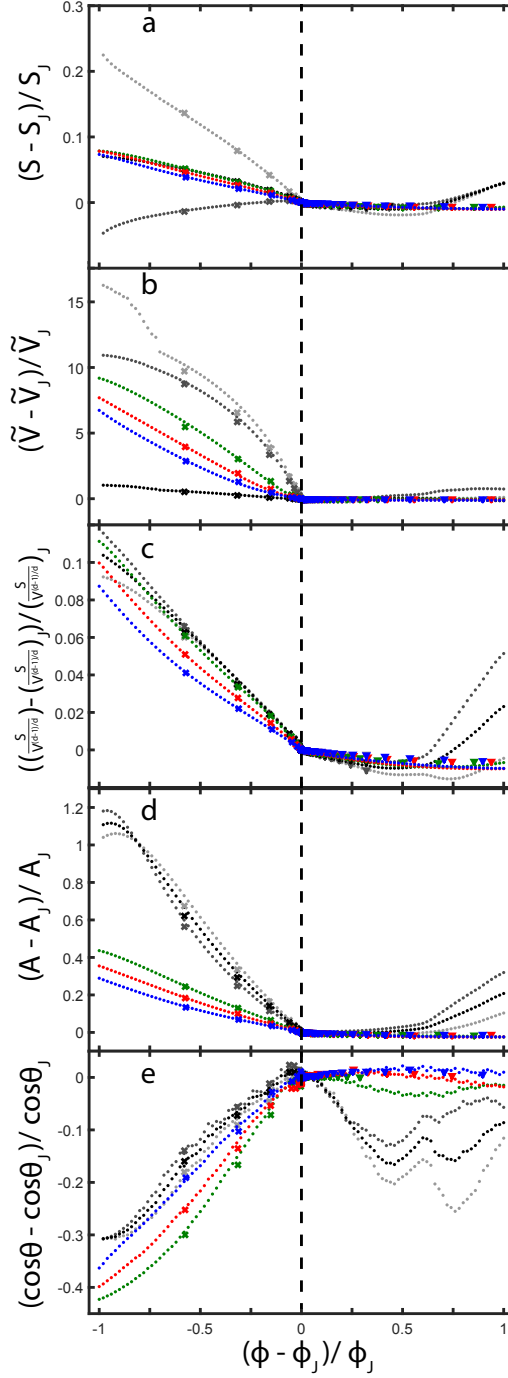


FIGURE 4. Plots of scaled order parameters vs. the scaled packing fraction. Closed circles represent IQ data, x's represent GM data (from below), and triangles represent ES data (from above). Note that on this linear scale the GM and ES data is nearly all clustered right at  $\phi_J$ . The parameters shown are (a) mean surface area,  $S$ , (b) standard deviation of volume divided by the mean of the volume,  $\tilde{V}$ , (c) mean surface to volume ratio  $S/V^{(d-1)/d}$  (d) mean aspect ratio,  $A$ , and (e) mean aspect ratio angle  $\cos\theta$ . We plot data for  $d = 2$  (smaller particles light gray, larger particles dark gray, combined black),  $d = 3$  (green),  $d = 4$  (red), and  $d = 5$  (blue).



Our three protocols differ only in how jamming is approached. All begin with a set of particles in random positions at a specified density. The energy of this system is then minimized to find the so-called inherent structure, found at the local energy minimum. Each of these protocols works as an iterative process by finding the inherent structure at a given density and then using this packing as the seed to find a minimized packing at a new density.

The **IQ protocol** begins with a random packing at zero density. Every particle is inflated to achieve a new packing at a specified higher density and this packings energy is then minimized. The results of this minimization are then used to create a denser packing, and so on. This proceeds in linearly spaced steps of packing fraction until the desired range of packing densities is covered. The range is chosen to cover densities from  $\phi = 0$  to  $\phi = 2\phi_J$ . The limits of this range are somewhat arbitrary but are chosen to be symmetric about  $\phi_J$ . While the most relevant region is near the transition point, we include data at both the high and low extremes for completeness. Data for  $d = 3 - 5$  uses 65536 ( $2^{16}$ ) particles, while  $d = 2$  uses 16384 ( $2^{14}$ ) particles.

The **GM protocol** is designed to zero in on the transition point, either approaching from above or below, without ever overshooting. In this manuscript, we only report on GM systems approaching from below because the ES protocol (described below) converges much faster when approaching from above. The GM protocol requires an initial bounding of the jamming point by choosing two densities, one above and one below. A packing is initially created at the lower bound and its energy minimized. A new packing is created between the upper and lower bounds using the original packing as its seed. If this packing is below jamming (taken to mean an energy per particle of  $< 10^{-20}$ ), it becomes the new lower bound and serves as the next seed. If, however, this packing is found to be above jamming it is discarded and its density is used as the upper bound in picking a new intermediate density. This proceeds until we approach the jamming point to within our energy per particle tolerance of  $10^{-20}$ . In this way we are able to create a packing right at the edge of jamming that is the result of only inflationary steps, without ever crossing into the jammed regime. Because the convergence is slow, we are only able to report on 8192 ( $2^{13}$ ) particles.

The **ES protocol** is limited in that it can only serve to approach jamming from above, but as previously mentioned, it converges faster than GM. The ES protocol exploits the scaling of system energy with excess packing fraction  $E \propto (\phi - \phi_J)^2$  to gently approach jamming from

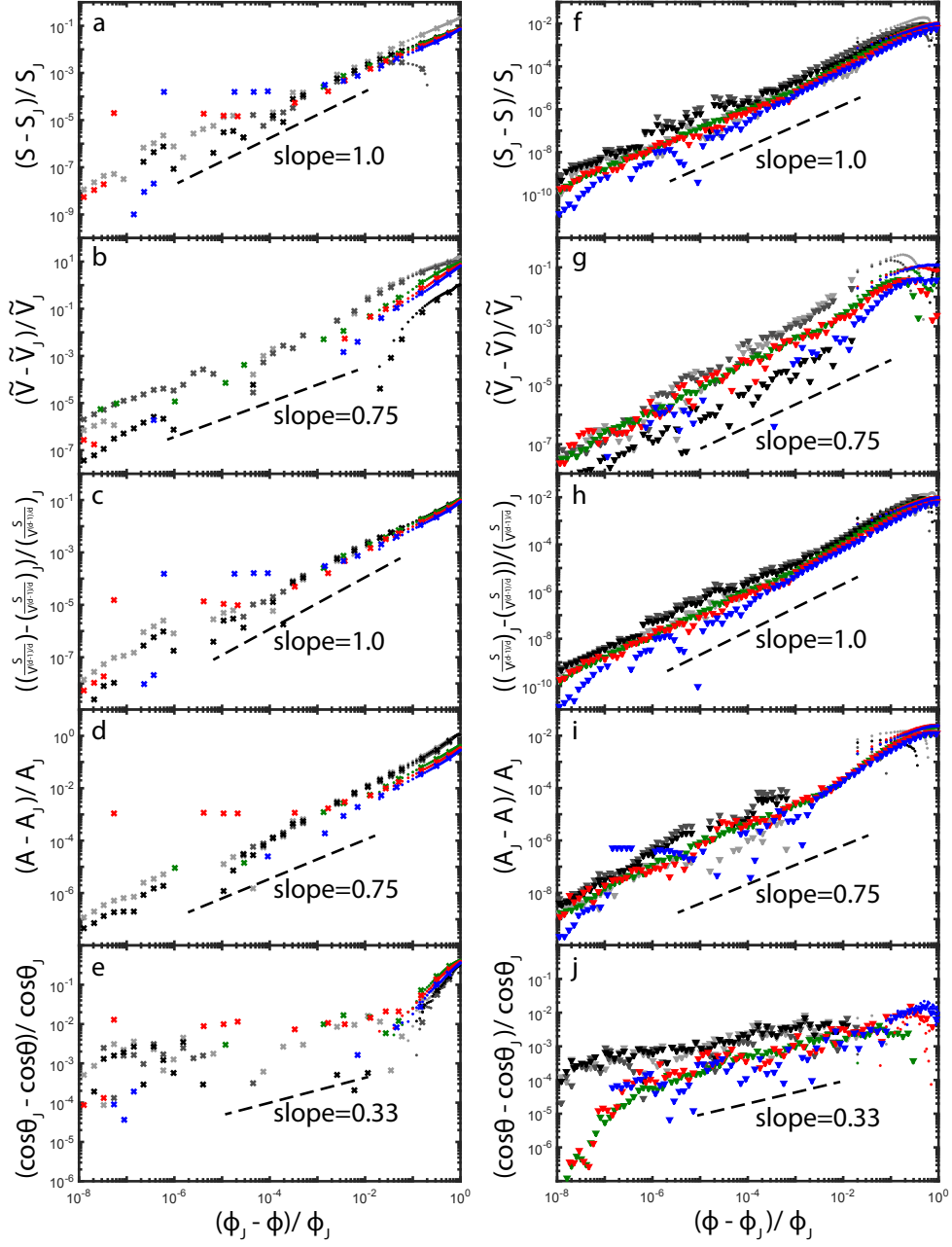


FIGURE 5. Log-log plots of each scaled order parameter vs. the scaled packing fraction approaching jamming from below (left) and above (right). Closed circles represent IQ data, x's represent GM data (from below), and triangles represent ES data (from above). The parameters shown are (a,f) mean surface area,  $S$ , (b,g) standard deviation of volume divided by the mean of the volume,  $\tilde{V}$ , (c,h) mean surface to volume ratio  $S/V^{(d-1)/d}$  (d,i) mean aspect ratio,  $A$ , and (e,j) mean aspect ratio angle  $\cos \theta$ . We plot data for  $d = 2$  (smaller particles light gray, larger particles dark gray, combined black),  $d = 3$  (green),  $d = 4$  (red), and  $d = 5$  (blue).

above, creating  $n_{\text{steps}}$  logarithmically spaced packings per decade. Given an initial system density  $\phi_i$ , system energy  $E_i$ , and a guess for the jamming density  $\tilde{\phi}_i$  we calculate the packing fraction for the next system as

$$\phi_{i+1} = \tilde{\phi}_i + (\phi_i - \tilde{\phi}_i) 10^{-1/n_{\text{steps}}}. \quad (3.1)$$

Once this new system's energy is minimized we compute a better estimate for the true jamming density as

$$\tilde{\phi}_{i+1} = \frac{\phi_{i+1} - \phi_i \sqrt{E_i/E_{i-1}}}{1 - \sqrt{E_i/E_{i-1}}}. \quad (3.2)$$

This process continues until we achieve an energy per particle of  $10^{-20}$ .

We choose the starting point of the approach to be approximately  $2\phi_J$ . It has been previously shown that the jamming density when approaching from above is dependent on the initial packing density for systems that start close to  $\phi_J$ . When the initial packing density is significantly high, however, the value of  $\phi_J$  is independent of the initial packing density [23]. We choose to start at such a high value of  $\phi$  to ensure that our results are independent of the starting density.

All ES data sets use 16384 ( $2^{14}$ ) particles. Data for  $d = 2$ ,  $d = 3$ , and  $d = 4$  are averaged over 10, 63, and 79 systems respectively while data for  $d = 5$  is taken from a single system.

### Geometry of the Voronoi tessellation

Given a packing created via any of our protocols and in any dimension we calculate the Voronoi tessellation using an in-house implementation of the algorithms described by Boissonnat and Delage [47] as used in our previous work [8] and extract the associated vertices using the Delaunay triangulation [48]. For the monodisperse packings we create in  $d = 3 - 5$ , this Voronoi tessellation is the standard Voronoi tessellation wherein the size of a cell is independent of the size of the particle. However, due to the bidispersity used in  $d = 2$  we use the radical Voronoi (or Laguerre) tessellation [7], which makes the boundaries between cells the bisecting plane between the particle edges. This preserves the convexity of each cell and thus provides a natural extension of the classical Voronoi cell. From each Voronoi cell, we extract all of our measurements. The

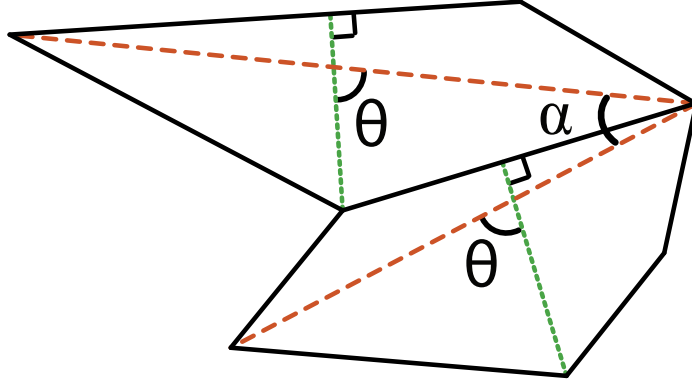


FIGURE 6. Illustration of the aspect ratio axes in two Voronoi cells. For each cell, the short axis is shown in green (short dashes) and the long axis is shown in orange (long dashes). The angle  $\theta$  between the two axes is defined to be the acute angle between the short and long axis. The angle  $\alpha$  between two long axes of different cells is also shown.

Parameter $\chi$	$N$	$S$	$\tilde{V}$	$S/V^{(d-1)/d}$	$A$	$\cos \theta$
Appx. Power $\gamma$	0.7	1.0	0.75	1.0	0.75	0.33
$\chi_J$ , $d = 2$ , large	6	3.00(5)	0.03(1)	3.73(8)	1.22(1)	0.56(7)
$\chi_J$ , $d = 2$ , small	6	2.27(5)	0.04(7)	3.82(7)	1.30(6)	0.55(9)
$\chi_J$ , $d = 2$ , all	6	2.64(0)	0.29(5)	3.78(2)	1.26(4)	0.56(3)
$\chi_J$ , $d = 3$	14.29	5.3(8)	0.03(8)	5.3(8)	1.32(2)	0.42(9)
$\chi_J$ , $d = 4$	32.74	6.8(7)	0.03(6)	6.8(8)	1.3(7)	0.38(5)
$\chi_J$ , $d = 5$	74.62	8.2(6)	0.03(4)	8.2(6)	1.4(1)	0.35(0)

TABLE 2. Scaling laws and critical values for all parameters  $\chi$ , such that  $\frac{\chi - \chi_J}{\chi_J} \propto \left(\frac{\phi - \phi_J}{\phi_J}\right)^\gamma$ . Critical values quoted have their error in the least significant digit, which is reported in parentheses. Both GM and ES data agree on each critical value. All critical values are unitless except for  $S_J$  which is reported as the unitless  $S_J N_{\text{particles}}^{(d-1)/d}$ . For  $d = 2$ , we report separately on  $\chi_J$  values for the larger particles, the smaller particles, and the system as a whole.

number of facets of the Voronoi tessellation gives us 1) the number of nearest neighbors  $N$ ; The vertices of the Voronoi cell allow us to calculate 2) the surface area  $S$  and 3) the volume  $V$ ; The ratio between the largest and smallest possible distances between parallel planes kissing the cell defines 4) the aspect ratio  $A$ ; Finally, the dot product between the headless vectors defining the aspect ratio provides 5) the cosine of the cell's internal angle  $\theta$ .

#### *Volume and Surface Area*

Volumes and surface areas can be calculated easily by breaking the cell into simplices. To find volumes and surface areas we exploit the fact that the  $d$ -dimensional volume of a  $d$ -simplex can be calculated from the generalized triple product of its vertices. The Delaunay triangulation

of the surface of a Voronoi cell breaks down the surface of each facet  $k$  into a number of  $(d - 1)$  dimensional simplices labeled by the index  $m$ . There are  $d$ -vertices association with each simplex, which we denote as  $\vec{v}_{m,i}$  where  $i$  ranges from 1 to  $d$ , and we denote the outward facing normal vector to a facet  $k$  as  $\hat{n}_k$ . From this, the surface area of each facet is calculated as the sum of the surface of all of its constituent simplices as

$$S_k = \sum_m \frac{|\hat{n}_k \cdot [(\vec{v}_{m,1} - \vec{v}_{m,d}) \wedge \cdots \wedge (\vec{v}_{m,d-1} - \vec{v}_{m,d})]|}{(d-1)!}, \quad (3.3)$$

where  $\wedge$  denotes the  $d$ -dimensional wedge product. The total surface area of a given Voronoi cell is then the sum of all facets

$$S = \sum_k S_k. \quad (3.4)$$

By choosing an interior point of the cell  $\vec{r}$ , we can subdivide the volume of the cell into a number of  $d$ -simplices whose volumes sum to the volume of the cell as

$$V = \sum_m \frac{|(\vec{v}_{m,d} - \vec{r}) \cdot [(\vec{v}_{m,1} - \vec{v}_{m,d}) \wedge \cdots \wedge (\vec{v}_{m,d-1} - \vec{v}_{m,d})]|}{d!}. \quad (3.5)$$

For a given packing, the mean cell volume is just the simulation volume divided by the number of particles. The distribution of cell volumes, however, does change, and so we report on  $\tilde{V}$ , the ratio of the standard deviation of the volume distribution to the mean. We also report on the mean of the unitless surface to volume ratio  $S/V^{(d-1)/d}$ .

#### *Aspect Ratio and Internal Angle $\theta$*

The ratio of surface area to volume  $S/V^{\frac{d-1}{d}}$  defines a simple notion of an aspect ratio, but one that is insensitive to the anisotropy of the cell. We define another aspect ratio, explicitly sensitive to anisotropy by looking at the ratio between the longest one dimensional span in a cell to the shortest one dimensional span of a cell (Figure 6). To calculate this aspect ratio we define

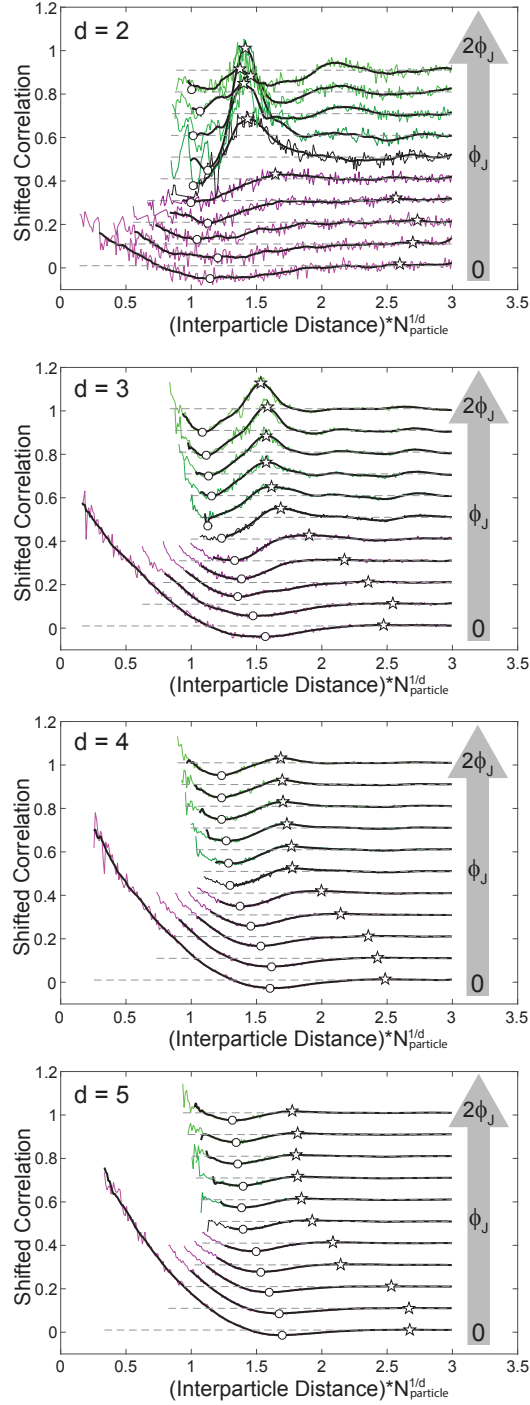


FIGURE 7. The normalized long axis correlation between Voronoi cells plotted as a function of distance between particles in  $d = 2 - 5$ . Correlations are shifted vertically to show the effect of changing  $\phi$  with a color scheme that fades from purple ( $\phi = 0$ ) to black ( $\phi = \phi_J$ ) to green ( $\phi = 2\phi_J$ ). Gray dashed lines show the line corresponding to completely uncorrelated axes, open circles denote minima and open stars represent secondary maxima. A black line has been drawn over each curve representing the Savitsky-Golay filter. Data obtained using the IQ protocol.

the long axis  $\vec{\ell}$  as the maximum distance between any pair of vertices and the short axis  $\vec{s}$  as the minimum of the set of maximum distances between each vertex and each facet. Given a set of vertices  $\vec{v}_i$  and introducing a point  $\vec{p}_k$  on each facet  $k$ , these definitions can be formalized as

$$\vec{\ell} = \{\vec{\ell} \mid \|\vec{\ell}\| = \text{Max}_{ij} \|\vec{v}_i - \vec{v}_j\|\}, \quad (3.6)$$

and

$$\vec{s} = \{\vec{s} \mid \|\vec{s}\| = \text{Min}_k (\text{Max}_i |\hat{n}_k \cdot (\vec{v}_i - \vec{p}_k)|)\}. \quad (3.7)$$

The aspect ratio is then simply defined as

$$A = \frac{\|\vec{\ell}\|}{\|\vec{s}\|}. \quad (3.8)$$

We can further measure the skewness of a cell by defining the angle between the long axis and the short axis as

$$\cos \theta = \frac{|\vec{\ell} \cdot \vec{s}|}{\|\vec{\ell}\| \|\vec{s}\|}, \quad (3.9)$$

where the absolute value is taken because  $\vec{\ell}$  and  $\vec{s}$  are headless vectors.

### *Correlation Function*

We can examine the interaction of each cell with its neighbors by defining a correlation function based on the angle between the axes of pairs of cells. When cells are packed together to fill space neighboring cells must share facets, potentially causing the axes to align. To characterize this we measure the cosine of the angle between two long axes  $\vec{\ell}_i$  and  $\vec{\ell}_j$  associated with particles  $i$  and  $j$  respectively (illustrated in Figure 6). Because the axes are headless vectors we must use the

formalism of directors, giving rise to the definition for the cosine as

$$\cos \alpha_{ij} = \frac{|\vec{\ell}_i \cdot \vec{\ell}_j|}{\|\vec{\ell}_i\| \|\vec{\ell}_j\|}. \quad (3.10)$$

To compare systems in different dimensions, we must first calculate the expectation values of completely uncorrelated directors. The expectation value of the cosine of the angle in dimension  $d$  is given by

$$\langle \cos \alpha \rangle_d = \frac{\int_0^{\pi/2} \cos \alpha \sin^{d-2} \alpha d\alpha}{\int_0^{\pi/2} \sin^{d-2} \alpha d\alpha} = \frac{\Gamma(\frac{d}{2})}{\sqrt{\pi} \Gamma(\frac{d+1}{2})}. \quad (3.11)$$

The standard deviation of the angle between uncorrelated directors in dimension  $d$  is defined as  $\sigma_d = \sqrt{\langle \cos \alpha \rangle_d^2 - \langle \cos^2 \alpha \rangle_d}$ . Therefore we also calculate the expectation of the square of the cosine of the angle of uncorrelated directors as

$$\langle \cos^2 \alpha \rangle_d = \frac{\int_0^{\pi/2} \cos^2 \alpha \sin^{d-2} \alpha d\alpha}{\int_0^{\pi/2} \sin^{d-2} \alpha d\alpha} = \frac{\Gamma(\frac{d}{2})}{2 \Gamma(d + \frac{1}{2})}. \quad (3.12)$$

Thus we find the standard deviation of uncorrelated directors in dimension  $d$  to be

$$\sigma_d = \sqrt{\frac{\Gamma(\frac{d}{2})^2}{\pi \Gamma(\frac{d+1}{2})^2} - \frac{\Gamma(\frac{d}{2})}{2 \Gamma(d + \frac{1}{2})}}. \quad (3.13)$$

We define our correlation function as the normalized value of the cosine of the angle between the long axes of every pair of particles as a function of the distance between cells as

$$C_\ell(r) = \sum_{ij} \delta(\|\vec{r}_i - \vec{r}_j\| - r) \frac{\cos \alpha_{ij} - \langle \cos \alpha \rangle_d}{\sigma(d)}. \quad (3.14)$$

We note that this correlation function, relating the shape and asymmetry of Voronoi cells, is logically distinct from the pair correlation function, or indeed from any correlation function based solely on particle positions.



## Analysis

### *Order Parameters*

Figure 19 presents the geometric order parameters described above calculated for systems created with all protocols as a function of distance to  $\phi_J$  for  $d = 2 - 5$ . Data across multiple dimensions is presented on the same scale by subtracting off the value at the jamming transition and then dividing by that same value. The packing fraction is similarly scaled as  $(\phi - \phi_J)/\phi_J$ . Below jamming all of these parameters change rapidly with increasing packing fraction. Jamming is marked by a sharp kink and above jamming they evolve with a much gentler slope.

For all measures except the surface area to volume ratio the  $d = 2$  data does not seem to collapse onto the same family of curves as the higher dimensions. Because the  $d = 2$  packings are bidisperse we show separate curves for each particle size (shown in dark and light gray) and a single curve representing the combined data (shown in black). The difference is especially apparent in the surface area: the Voronoi surface area increases for larger particles and decreases for smaller particles as jamming is approached from below. This makes intuitive sense; at extremely low packing fractions the Voronoi cells for the two sets of particles should be almost identical and near jamming the larger particles will end up having a larger surface area and a larger volume than their smaller counterparts. In the combined data, the surface area curve collapses to follow the trend observed in  $d = 3 - 5$ , which is somewhat surprising considering the very significant geometric structure of bidisperse packings versus monodisperse. However, when considering each size separately, this universality is broken. For completeness we provide data on 3d bidisperse systems in the supplementary material. These 3d bidisperse systems do not always exhibit the same behavior as monodisperse systems, however they always show power-law scaling when approaching jamming.

In order to explore the behavior very close to jamming we use the GM protocol to approach from below and ES to approach from above. In this way we obtain packings that converge logarithmically on  $\phi_J$ . Plotted on a log-log scale (Figure 20) we find that each parameter scales with its own power-law on both sides of the transition with power law values and critical values listed in Table 2. We have previously demonstrated that the mean number of neighbors  $\langle N \rangle$  scaling is consistent with a power of  $\sim 0.7$  [8].

Below jamming, there must be a limit to the scaling regime. The mean surface area  $\langle S \rangle$ , volume  $\langle V \rangle$ , and number of facets  $\langle N \rangle$  of Voronoi cells at  $\phi = 0$  and their respective dimensional dependence can be semi-analytically determined [35, 49–51]. The same should be true for aspect ratio  $\langle A \rangle$  and internal angle  $\langle \cos \theta \rangle$  but to our knowledge those studies have not yet been done. This is responsible for the changes in curvature seen at low  $\phi$  in Figure 19.

While most of the power laws work well over at least five decades, there are a few exceptions. The data from below is very sparse, and so we cannot claim that the power laws fit exactly and can only suggest that the plots look like power-laws within the plotting area. Precise claims about the scaling exponents of these power laws would require a method which approached jamming more predictably from below and which converged much faster so that averaging could be used, as it is done above jamming.

It is also important to note that the  $d = 2$  data deviates significantly in the standard deviation of the volume for particle sizes considered separately (Figure 20g) and the internal angle for all cases (Figure 20j). What is unclear is the extent to which this non-universal behavior is due to the dimension or the bidispersity. We can probe this question by examining the  $d = 3$  bidisperse system which is presented in the supplement. Unlike the  $d = 2$  bidisperse system, the  $d = 3$  case shows non-universal behavior even in the combined statistics. This suggests that the fault lies in the polydispersity and perhaps not the dimension as was claimed in our earlier work [8]. It is not surprising that adding polydispersity will change the behavior of these detailed geometric properties. The result is that it is impossible to decouple the effects of polydispersity from those of dimension in causing the non-universal  $d = 2$  behavior.

### *Correlation Function*

From the measurements of the aspect ratio we can see that at jamming the Voronoi cells are much more isotropic than they are far from jamming. At jamming, the aspect ratio is close to 1 and the direction of the long and short axes are uncorrelated as measured by  $\cos \theta$ . In contrast, at very low density the cells are elongated and have a large aspect ratio and axes that are nearly perpendicular. Figure 7 shows the measured correlation function between the long axes as a function of interparticle distance for packing fractions ranging from  $\phi = 0$  to  $\phi = 2\phi_J$  in dimensions  $d = 2 - 5$ . Far below jamming, neighboring particles are highly correlated. This

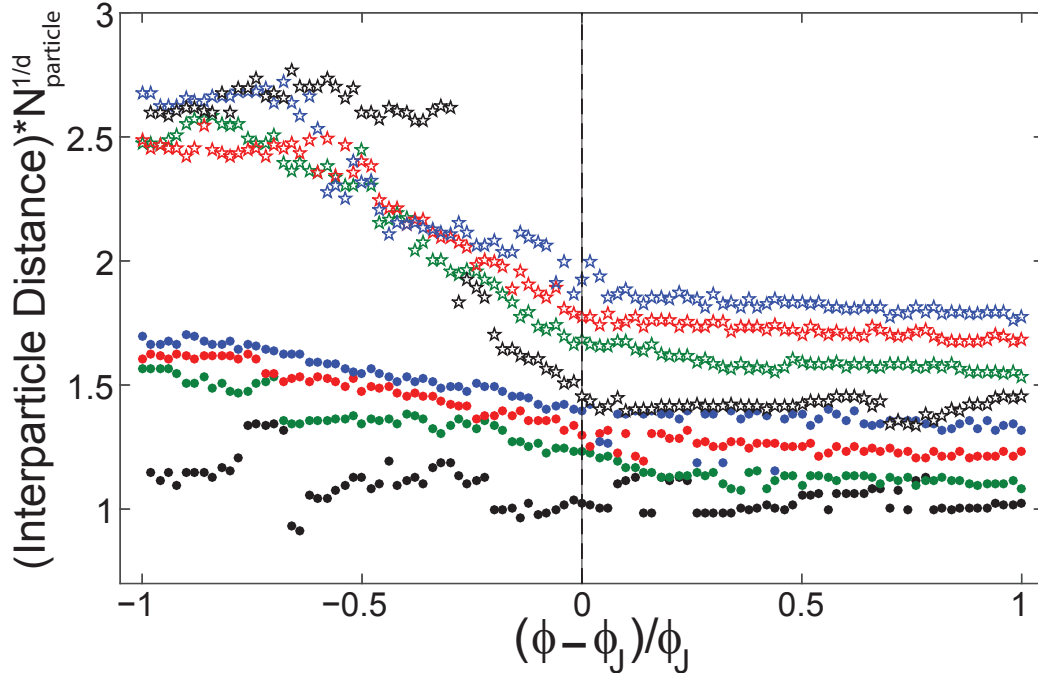


FIGURE 8. The position of the minimum (closed circles) and secondary maximum (open star) of the correlation shown in Figure as a function of distance from the jamming transition. Colors shown represent dimensions 2 (black), 3 (green), 4 (red), and 5 (blue).

correlation decreases with increasing distance, showing an anti-correlated dip at intermediate distances and then finally decaying to completely decorrelated at large distances. At jamming, the correlation function changes qualitatively, marked by the appearance of a positive correlation peak at intermediate distances in addition to the short distance dip. Both the dip and the peak become more prominent and sharpen at higher packing fractions. These extrema are found using a cubic Savitzky-Golay filter with a span of 51 data points [52] and the positions of the dip and peak are indicated by circles and stars respectively in Figure 7 and plotted as a function of packing fraction in Figure 8. The position of the maximum shows a clear signature of the transition in  $d = 2 - 5$ . However, the position of the minimum for  $d = 3 - 5$  does not show a clear signature of this transition. We find that the correlation functions plotted in Figure 8 only depend on interparticle distance, with no angular dependence when oriented to the long axes of each given particle. This correlation function is unusual in that the jamming transition is marked by the disappearance of the nearest neighbor correlation, seen in the value of the correlation function at the shortest possible interparticle distance.

## Conclusion

We have observed a clear signature of the jamming transition in each of the studied measures of the Voronoi cell as well as in our newly defined axis-correlation function. These results bolsters the claim that while jamming is a mechanical transition, it can be viewed separately as a purely geometric phenomenon via the Voronoi cells. These results justify the use of the Voronoi cell as a tool to understand the jamming transition. Ultimately, each of the measures are sensitive to the fluctuations in the size and shape of individual Voronoi cells. Each measure reflects a different change in the cell. The fact that we see power-law scaling in all of these measurements, even in 2d bidisperse systems (albeit with different exponents), suggests that nearly every aspect of the cell changes and is controlled by the transition from unjammed to jammed. Our results demonstrate that the mechanical jamming transition coincides perfectly with a transition in the geometry of the packing at  $\phi_J$ .

## Acknowledgments

We thank John Royer for helpful discussions. This work was supported by the NSF under Career Award DMR-1255370. The ACISS supercomputer is supported under a Major Research Instrumentation grant, Office of Cyber Infrastructure, OCI-0960354.

## CHAPTER IV

### HIDDEN SYMMETRIES IN JAMMED SYSTEMS

#### **Abstract**

There are deep, but hidden, geometric structures within jammed systems, associated with hidden symmetries. These can be revealed by repeated transformations under which these structures lead to fixed points. These geometric structures can be found in the Voronoi tessellation of space defined by the packing. In this paper we examine two iterative processes: maximum inscribed sphere (MIS) inversion and a real-space coarsening scheme. Under repeated iterations of the MIS inversion process we find invariant systems in which every particle is equal to the maximum inscribed sphere within its Voronoi cell. Using a real-space coarsening scheme we reveal behavior in geometric order parameters which is length-scale invariant.

This work is unpublished, but has been accepted into the Journal of Statistical Mechanics: Theory and Experiment. Eric Corwin advised all of this work and so he is added as a coauthor, but the majority of the work and writing was my own.

#### **Background**

The jamming of athermal spheres has been called the epitome of disorder [6], but this doesn't mean that it is devoid of all symmetries. The structure found within jammed systems distinguishes them from Poisson point processes, for which there is no structure or correlation. This structure is reflected in the non-trivial behavior of correlations (such as the pair-correlation function) [53, 54], geometry [8, 9], contact number distributions [55], hyperuniformity [20, 56], and volume distributions [26, 57]. Recent theoretical work has demonstrated the existence, and breaking of an abstract replica symmetry at the jamming and glass transitions, namely liquid systems have replica symmetry and glasses or jammed systems break that symmetry. [1, 58]. In this work we search for evidence of hidden symmetries in the spatial and geometric structure of systems below, at, and above jamming. We employ the general scheme of repeated transformations in the hope that they will lead to fixed point systems reflective of the underlying symmetries.

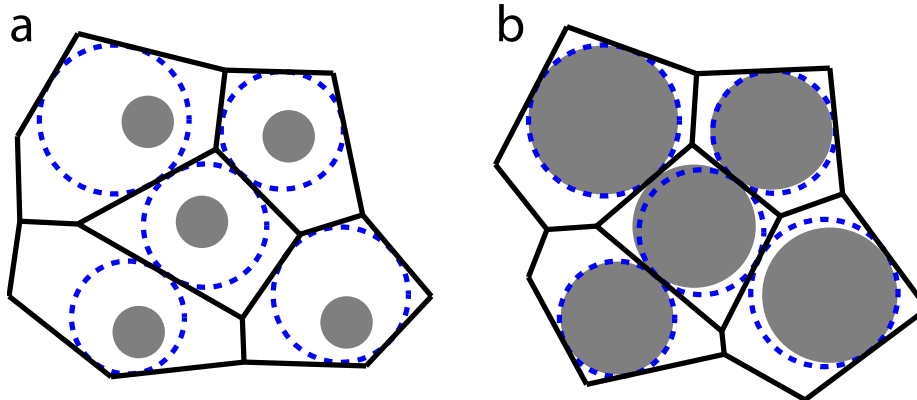


FIGURE 9. Diagram showing the maximum inscribed sphere (MIS) inversion. (a) An initial monodisperse packing is shown with particles colored gray, their radical Voronoi cells in black, and the MIS shown as a dashed blue line. (b) The first step of the MIS inversion with the same color scheme. Note that the MIS from (a) is the new particle, the Voronoi cell has changed, and the system is now polydisperse.

We have previously shown that a number of geometric properties of the Voronoi tessellation carry signatures of the jamming transition, including the number of neighbors, surface area, volume, aspect ratio, and maximum inscribed spheres (MIS). There is an obvious symmetry that jumps out precisely at the jamming transition. Because each particle in a jammed system is in contact with several of its neighbors it must kiss the boundaries of its Voronoi cell. Therefore, the maximum inscribed sphere of a Voronoi cell must be equal to the particle. This suggests a transformation of repeatedly replacing every particle with the maximum inscribed sphere of its Voronoi cell. Under such a transformation, jamming will necessarily be a fixed point.

The renormalization group has been very successful in understanding phase transitions. At present, jamming lacks an appropriate field with which to construct a renormalized field theory. Nevertheless, we barrel ahead with a brute force real space coarsening and rescaling scheme in the hopes of pointing the way to the appropriate field theory. By repeated iteration of this coarsening we test a range of geometric order parameters to see if they mimic the behavior of a proper renormalized field.

## Methods

### *Packing Simulations*

In order to generate the initial packings for our MIS Inversion and coarse graining, we use an infinite temperature quench protocol [15] as described in reference [8]. The process begins with uniformly randomly distributed athermal frictionless particles with monodisperse or polydisperse radii chosen to achieve a desired packing fraction. The packing fractions for monodisperse packings are chosen within the range  $\phi = 0$  to  $\phi = 2\phi_J$  (where  $\phi_J$  is the packing fraction at jamming) to obtain the full spectrum of behavior, both well below and well above jamming. Polydisperse packings are generated with densities from  $\phi = 0$  to significantly above  $\phi_J$  but not all the way to  $2\phi_J$ . We choose a harmonic contact potential between particles and then allow the system to relax to its local potential energy minimum (also called its inherent structure) via the conjugate gradient algorithm [32] for systems below  $\phi_J$  or the fast inertial relaxation engine (FIRE) algorithm [33] for systems above  $\phi_J$ . For studies of the MIS Inversion we use monodisperse packings of 8192 particles and polydisperse packings of 16384 particles. Coarse graining requires higher numbers of particles, and so we use monodisperse systems that contain 65536 particles. All data is monodisperse unless otherwise stated.

For polydisperse packings, we choose radii from a log-normal distribution. We characterize a polydisperse packing by the standard deviation of the radii divided by the mean. For the MIS inversion, we report on initial polydispersities of 0, 0.05, 0.1, 0.15, and 0.2.

### *Geometric Cell Properties*

The maximum inscribed sphere (MIS) of a Voronoi cell is the largest sphere that is fully contained within the boundaries of the cell. It is calculated using linear programming techniques [59].

Detailed descriptions of how we calculate the number of neighbors, the surface area, the volume, and the aspect ratio can be found in our previous work [8, 9]. Two particles are considered neighbors if their Voronoi cells share a facet, so to find the number of neighbors, we calculate the number of facets via a method developed by Boissonnat [47]. To find the surface area and the volume, we calculate the vertices of each cell and take a delaunay triangulation to

split each facet into simplices. From these simplices and an interior point of the cell, it is simple to calculate the surface area and volume associated with each cell.

The aspect ratio that we use for convex cells is defined by the maximum distance between any pair of vertices contained in a cell divided by the minimum of the maximum distance between each vertex and every facet. Thus, the aspect ratio can be seen as the ratio between the longest and shortest spanning lengths of a cell.

### *Maximum Inscribed Sphere Inversion*

The MIS inversion process starts with a sphere packing at any density. From this packing we calculate the radical Voronoi tessellation (also sometimes called the Laguerre tessellation). We choose to use the radical Voronoi tessellation as opposed to the additively-weighted Voronoi tessellation (or indeed any other tessellation) to ensure that the Voronoi cells are always convex regardless of polydispersity [7]. From this tessellation we calculate the MIS for each cell. Finally, this new set of spheres is treated as a new sphere packing upon which we can iterate this procedure. We note that each MIS is in general uniquely determined, with the exception of the pathological case in which there is a high degree of symmetry in the underlying Voronoi cell (for example, if the cell is a rectangular solid). This pathological case will not happen in a disordered system, and so we do not explicitly account for it. However, even if such cases were present they would simply manifest as a degenerate set of spheres, of which our analysis would choose one.

We find that for all systems this process converges to a fixed point packing, dependent on the initial input. In practice, we find that repeating this process 30 times is sufficient to find fixed points in which each particle deviates by less than one part in  $10^6$  from its former position, as shown in figure 10a.

Even though the MIS inversion constructs packings that are guaranteed to have no overlaps we can still define a coordination number  $z$  for each particle by choosing an appropriate cutoff distance. We pick this distance to fall immediately after the first peak in the pair-correlation function.



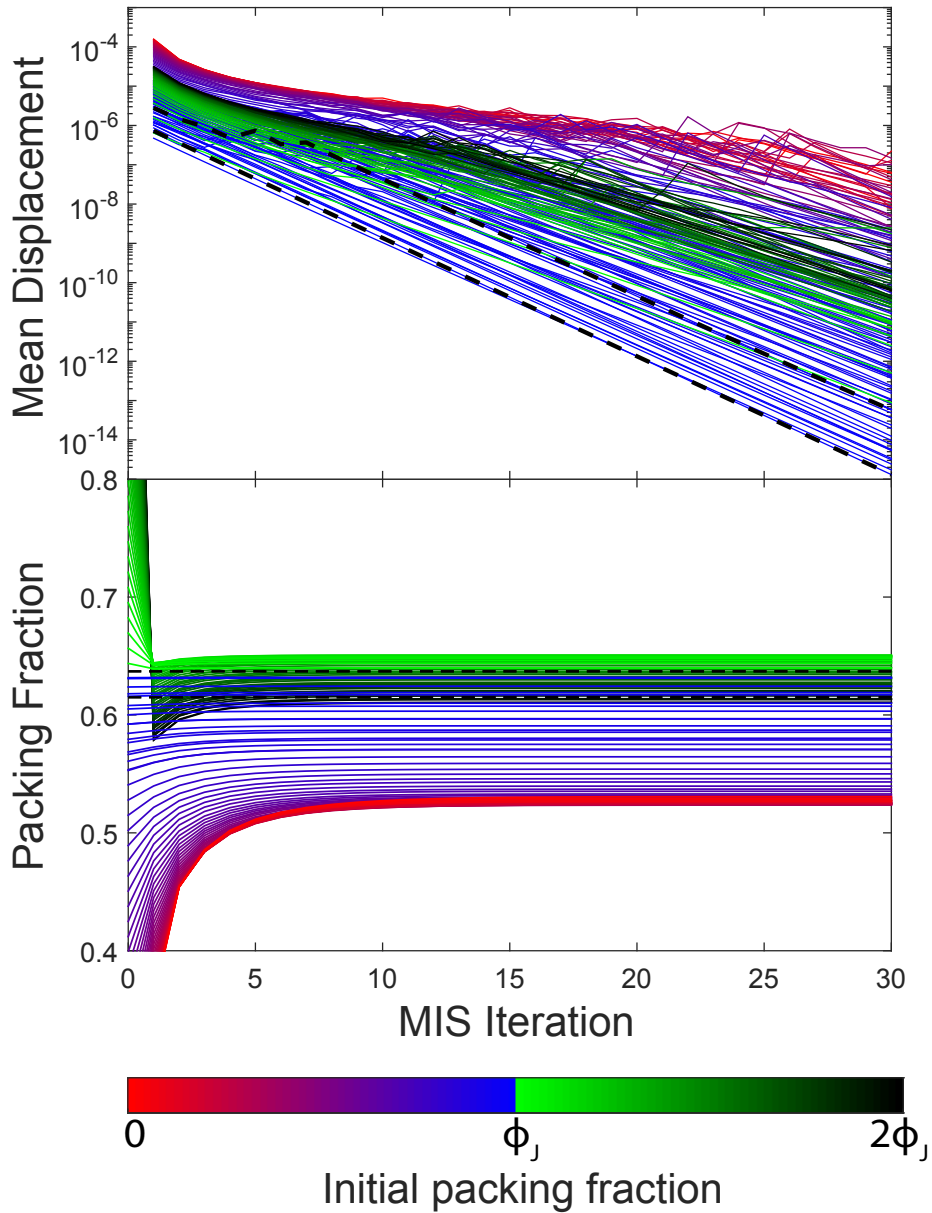


FIGURE 10. Convergence of the MIS inversion. a) Log-linear plot of the mean displacement per particle from the previous MIS iteration. Each line represents a system at a different initial packing fraction, with color scale indicating initial packing fraction as shown beneath the plots. The lower dashed line is drawn at  $\phi_J$  and the upper dashed line is drawn at  $\phi^*$ , the lowest packing fraction for which initial packings are fixed points under the MIS inversion. b) Packing fraction at each step of the MIS inversion, using the same color scheme as a. The upper dashed line is drawn here at  $\phi_J$  and the lower dashed line is at  $\phi^*$ , which is flipped from a.

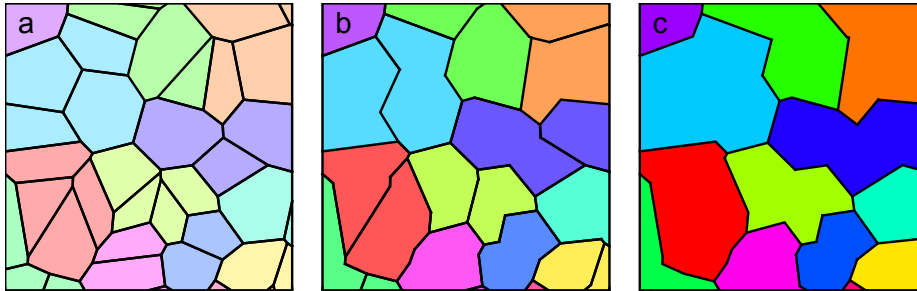


FIGURE 11. The coarse graining procedure pairs each cell in with the unpaired cell that shares the highest surface area. a) The original Voronoi diagram, b) the system after one step of the coarsening procedure, c) the system after two steps of coarsening. Colors denote the membership in cells after two rounds of coarsening.

### *Real-Space Coarsening*

Given a sphere packing at any density, we compute the Voronoi tessellation and the geometric cell properties, defined above. Because the systems under study here are monodisperse it doesn't matter which Voronoi tessellation we choose, as they are all degenerate. Our real space coarsening scheme creates a coarser grained packing by joining pairs of neighboring cells. To do so, we choose a random ordering of cells and sequentially pair each cell in our list with the the unpaired neighboring cell that shares the largest interfacial surface area. Both cells are then removed from the list, and the process continues until nearly all cells are paired. Because of the random nature of this process there will always be a few singleton cells remaining which we join with the previously paired cell with which it shares the highest interfacial surface area (with the caveat that no composite cell can be made up of more than three cells). These triplet cells constitute less than 3.5% of the total cells in  $d = 3$ , 1.7% in  $d = 4$ , and 0.7% in  $d = 5$ . The set of paired cells covers all space and thus produces a new tessellation. Note that this new tessellation is *not* a Voronoi tessellation and is not even convex. However, our pairing scheme is designed to create cells that are compact and nearly convex upon high iterations. We continue this process iteratively to create a further new tessellation with approximately half as many cells as the previous one. Thus the number of iterations possible in this scheme is limited by the number of particles in the initial packing. In  $d = 3$ , we average this process over 100 different orderings. In  $d = 4$ , we use one ordering due to the increased computation time.

If we label two neighboring cells  $A$  and  $B$  we can call the combined cell  $A \cup B$ . The neighbors of  $A \cup B$  are the union of the set of neighbors of  $A$  and  $B$  (not counting each other),

the volume is simply the sum of the constituent volumes, and the surface area is the sum of the constituent surface areas minus twice the interfacial surface area. Because the new cells are not convex and our aspect ratio only applies to convex cells, we take the convex hull of the vertices of all the constituent cells and we calculate the aspect ratio as defined above. This preserves the definition that the aspect ratio is the longest one dimensional distance divided by the shortest one dimensional distance, but these two distances are no longer constrained to be fully contained within the cell.

When a combined cell is made of three constituent cells  $A$ ,  $B$ , and  $C$ , this process is done for  $A \cup B$  and then  $(A \cup B) \cup C$ .

## Discussion

### *Maximum Inscribed Sphere*

Under repeated action of the MIS inversion, we find that every initial packing quickly reaches a fixed point depending only on the initial packing fraction and initial polydispersity. Figure 12a plots the asymptotic polydispersity against the asymptotic packing fraction. Each curve shown corresponds to a different starting polydispersity, ranging from 0 to 0.2, in steps of 0.05, with varied initial packing fraction from  $\phi = 0$  to  $\phi = 2\phi_J$  represented by the color scale. These fixed points form a continuous line in this phase space, demonstrating that packings with similar initial properties to one another transform into fixed point packings with similar asymptotic properties.

The presence of rattlers (particles which are unconstrained, even in a jammed system) induces a small drift between the initial packings and fixed point packings, even at  $\phi_J$ . If we were to apply this same transformation in higher dimensions where the presence of rattlers is greatly diminished [23], we expect that the points would correspondingly drift even less.

By design, jammed packings at  $\phi_J$  are a fixed point under this repeated transformation. We find that systems extending a significant distance below jamming are also fixed points. Surprisingly, this extends down to a density consistent with our previously discovered  $\phi^*$  [8]. This is the point at which the distribution of MIS radii first becomes a delta function. The values used for  $\phi^*$  are 0.615 and 0.427 in  $d = 3$  and  $d = 4$  respectively. However, we find that the mean coordination number in dimension  $d$  jumps from  $d + 1$  to  $2d$  not at  $\phi^*$ , but at  $\phi_J$ , which

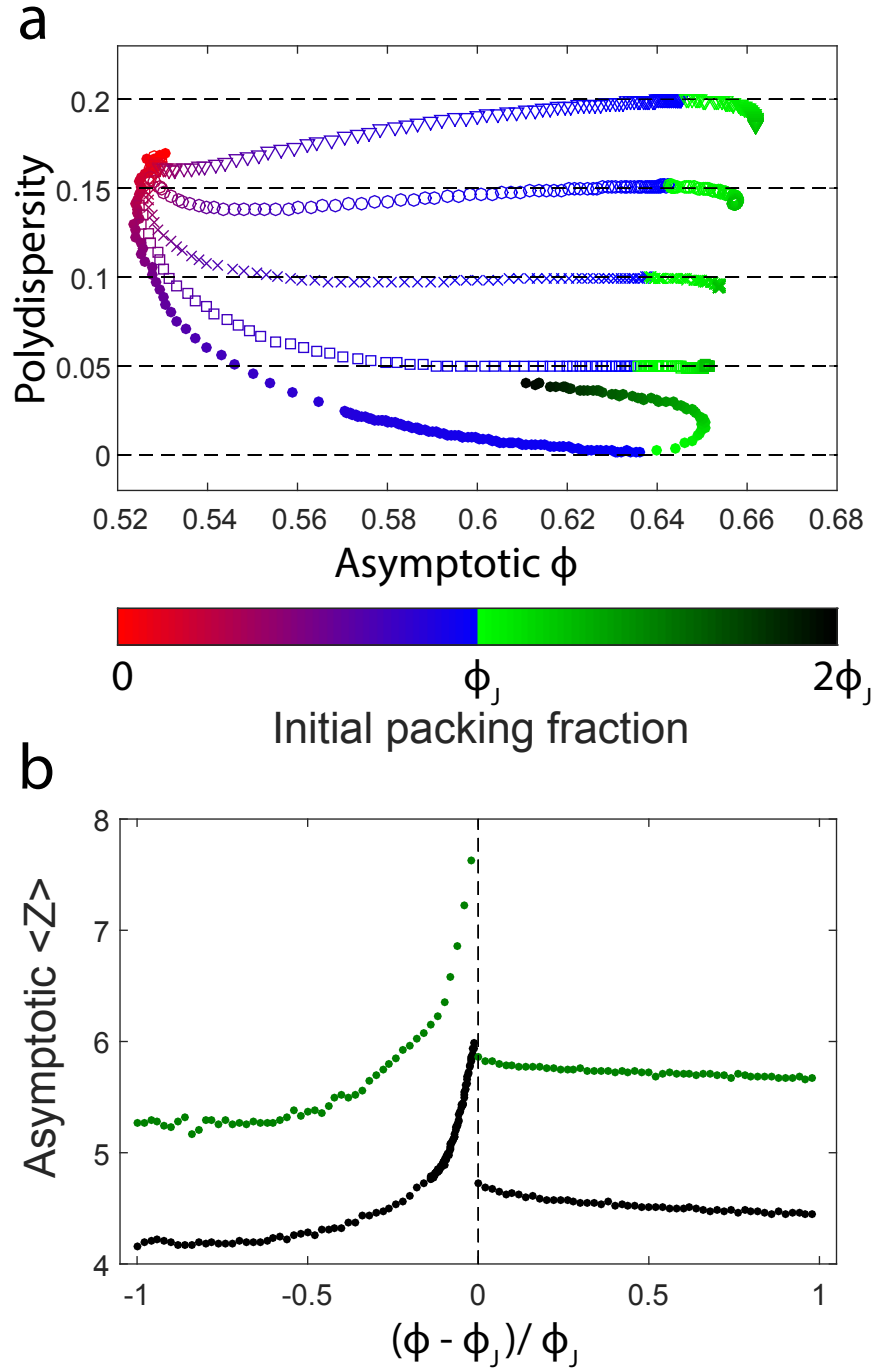


FIGURE 12. Asymptotic properties of the MIS inversion. a) Fixed points of the MIS Inversion are represented by their polydispersity and their final packing fraction. Initial packings start at polydispersities of 0 (closed circles), 0.05 (squares), 0.1 (x's), 0.15 (open circles), and 0.2 (triangles). Points that remain fixed through the entire process lie on the dotted lines associated with their starting polydispersity. Initial packing fraction is coded into the color. b) Asymptotic mean number of contacts  $\langle Z \rangle$  as a function of initial packing fraction for  $d = 3$  (black), and  $d = 4$  (green).

simply indicates that the particles in this range are not jammed. The fact that systems between  $\phi^*$  and  $\phi_J$  are fixed points of this transformation points conclusively to a symmetry that exists only within this range: all non-rattler particles are exactly equal to the MIS of their Voronoi cells.

Systems that begin well above jamming get folded back to systems below jamming under this transformation. This is because the MIS of a Voronoi cell for an overjammed particle is always smaller than the particle itself due to the fact that overjammed particles are not fully contained within their Voronoi cells [8]. These systems always appear to be folded onto the range between  $\phi^*$  and  $\phi_J$ .

We observe a cluster of data points near an asymptotic  $\phi = 0.53$ , with no fixed points falling below this density. This packing fraction is strikingly similar to those obtained in frictional random loose packing (RLP) experiments and simulations [2, 60]. Further, these fixed points all have a mean coordination number of  $\langle Z \rangle \simeq 4$  in  $d = 3$  (shown in figure 12b), as required for RLP. By design, each MIS particle must have a minimum of  $Z = d + 1$  non-cohemispheric contacts, but this only sets a lower bound. Thus, these fixed point packings appear to be a frictionless analog of RLP. In this way, MIS inversion offers an interesting, non-physical mechanism for generating polydisperse RLP packings. It would be interesting to compare the same process in higher dimensions to high dimensional simulations of RLP if they were to become available.

### *Real-Space Coarsening*

For all of the parameters studied, our systems reach fixed points under appropriate rescaling after only a few iterations of the coarsening procedure. However, the shape of the curve of fixed points appears to be strongly dependent on the parameters in question. Figure 13a-d shows the iterative application of the coarse graining to a range of systems between  $\phi = 0$  and  $\phi = 2\phi_J$  in  $d = 3$  for the mean number of neighbors (a), the mean surface area (b), the standard deviation over the mean of the volume (c), and the mean aspect ratio (d). Figure 13e-h shows just the original order parameter and the fixed point after 6 iterations of the coarsening for  $d = 3$  and  $d = 4$ , showing similar behavior across dimension.

The mean number of neighbors (Figure 13 a,e) retains its shape most closely, but is highly susceptible to noise, as each cell can only have an integer number of neighbors. The volume graph (Figure 13 c,g) appears to be even more susceptible to noise, as the standard deviation

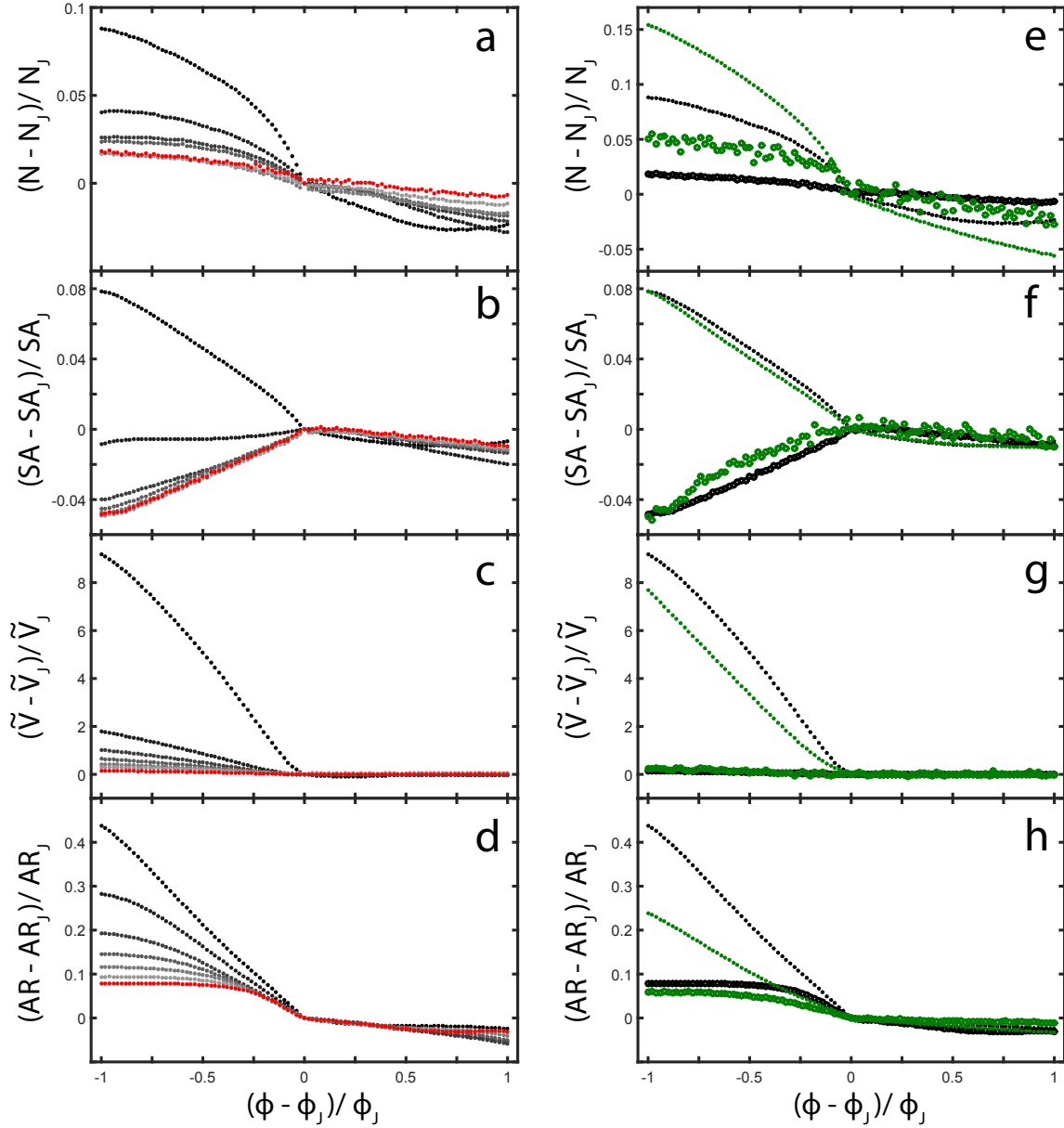


FIGURE 13. Under the coarse graining scheme, the behavior of each parameter of the cells reaches a curve of fixed points as a function of packing fraction. On the left, we have plotted the initial parameter (black) and the first 6 coarse grainings (each corresponding to a lighter shade of gray, with the 6th in red) in three dimensions for the mean number of neighbors (a), mean surface area (b), standard deviation over the mean of volume (c) and aspect ratio (d). In each, we scale by subtracting off and dividing by the order parameter at  $\phi_J$  in that iteration, such that the jamming point is always at the origin. On the right (e-h), we have plotted only the original (closed circles) and the 6th iteration (open circles) for  $d = 3$  (black) and  $d = 4$  (green).

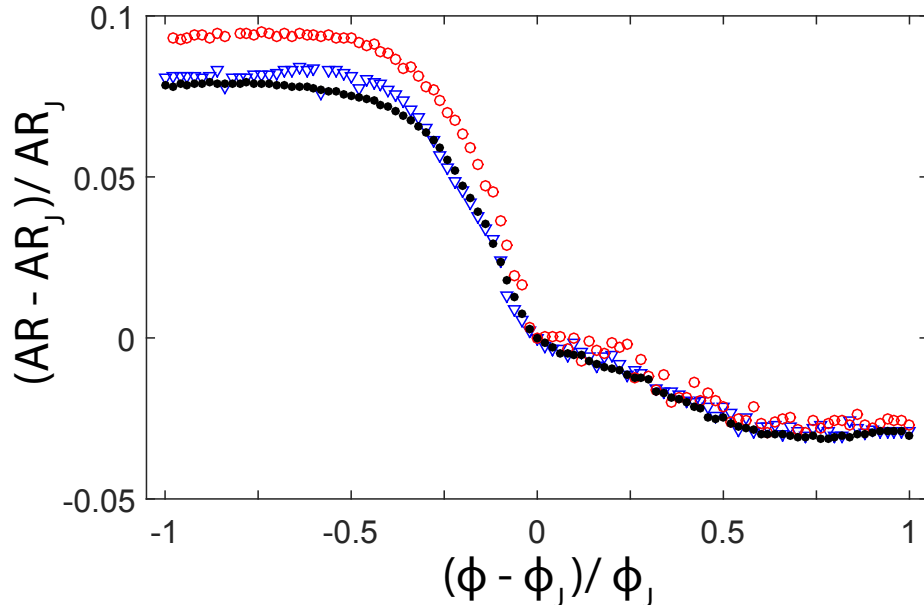


FIGURE 14. Coarse grained aspect ratio cross over shows no evidence of finite size effects. We have plotted 3 system sizes in  $d = 3$  at the 6th iteration of the coarsening (as done in figure 13h), with system sizes of 4096 (red open circles), 8192 (blue triangles), and 65536 (black closed circles).

over the mean goes to zero upon even modest iterations of the process. It is the surface area and the aspect ratio which show the strongest and most interesting behavior. The surface area (Figure 13 b,f) appears to come into the transition linearly at first, but after the transformation, the trend reverses itself and quickly reaches a fixed point that is almost a mirror of the original. Interestingly, each packing fraction retains perfect memory of where it began before the iterations. The same statement about memory could possibly be said for the neighbors if the graphs weren't so susceptible to noise.

The aspect ratio (Figure 13 d,g) gives us the strongest signature of the jamming transition under repeated iterations of the coarse graining. We observe that at high iterations of the process we get one value of the aspect ratio far below jamming and one value above jamming. There is a cross-over region which may be related to the pre-jamming phase transition that occurs at  $\phi^*$ , as the halfway point seems to coincide with the numerical values used for  $\phi^*$ . By examining this behavior as a function of system size in figure 14 we can conclude that this extended cross-over regime is not merely the finite size blunting of a step function. Indeed, there is very little change at all between systems of 4096 particles and those of 65536.

## Conclusion

Each of these transforms provide a new perspective towards understanding jammed systems. Through the MIS inversion, we have clarified the pre-jamming phase transition at  $\phi^*$ . Systems between  $\phi^*$  and  $\phi_J$  are fixed points of the inversion, meaning that they exhibit a symmetry wherein the MIS is equal to the particle itself. This symmetry is interesting in that it relates the real particles to the Voronoi network, which is a purely geometric construct. We posit that the transition at  $\phi^*$  can only be seen when observing an order parameter that is influenced both by the mechanical network of contacts as well as the geometric Voronoi cell. Thus, it is perhaps not surprising that this pre-jamming transition is absent in purely mechanical or purely geometric order parameters. It is interesting to note that the value of  $\phi^*$  is very close to the value of the ideal glass transition in thermal hard spheres [61]. We are actively pursuing this line of research.

The coarse graining reveals a different symmetry which could be useful in constructing a renormalizable field theory for jamming. Both the surface area and the aspect ratio present interesting features under coarse graining which preserve knowledge of the underlying packing while other features are washed out. Somehow, the surface area retains perfect memory of the underlying packing. Aspect ratio is particularly intriguing as it separates systems into two clearly different classes, above and below the jamming transition. This is reminiscent of the renormalization group's delineation between relevant and irrelevant graphs. If this can be translated into a rigorous renormalization group analysis, it would imply that either the surface area, the aspect ratio, or both reveal symmetries that fundamentally differentiate a jammed packing from an unjammed one.

## Acknowledgments

This work was supported by the NSF under Career Award DMR-1255370. The ACISS supercomputer is supported under a Major Research Instrumentation grant, Office of Cyber Infrastructure, OCI-0960354.



CHAPTER V

SUPPLEMENTARY MATERIAL FOR CHAPTER 2

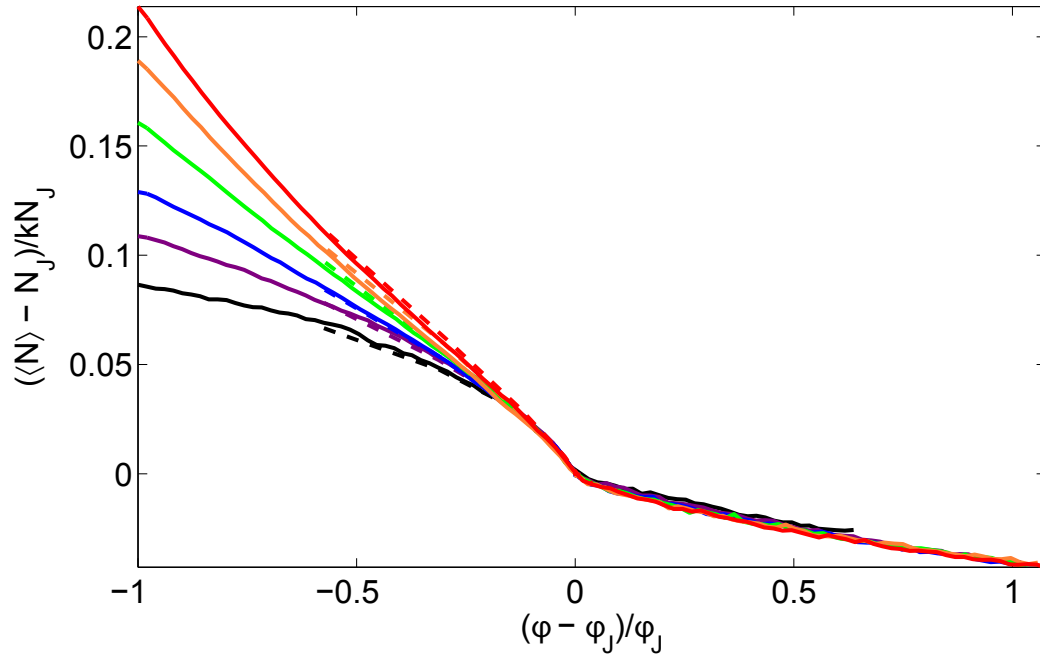


FIGURE 15. Scaled mean number of neighbors vs. scaled packing fraction for various packing protocols. Solid lines represent Infinite Quench data and dashed lines represent Geometric Mean search data. The same values for  $\phi_J$ ,  $N_J$ , and  $k$  are used for collapse in each dimension. In general it is not required that we use the same parameters, but we have done so to show how strong the agreement is between the methods used to approach jamming. Shown are  $d=3$  (black), 4 (purple), 5 (blue), 6 (green), 7 (orange), 8 (red).

Dim	$\phi^*$	$\phi_J$ below	$\phi_J$ above
3	0.6150	0.6372	0.6472
4	0.4270	0.4517	0.4636
5	0.2820	0.3031	0.3155
6	0.1792	0.1965	0.2066
7	0.1115	0.1238	0.1309
8	0.0672	0.0758	0.0809

TABLE 3. Table of values for  $\phi^*$ , and  $\phi_J$  used in this manuscript. Note that there are a range of values for the jamming transition dependent on method.

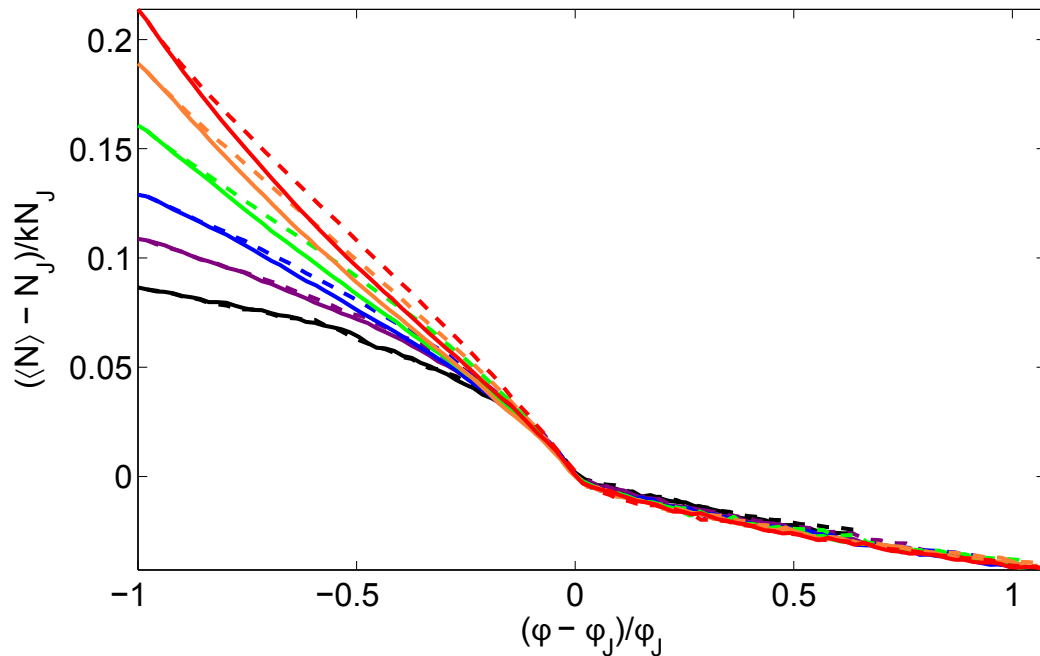


FIGURE 16. Scaled mean number of neighbors vs. scaled packing fraction for various packing protocols. Solid lines represent Infinite Quench data and dashed lines represent a simulated annealing wherein each point represents a dilation from the previous data point followed by an energy relaxation. The same values for  $\phi_J$ ,  $N_J$ , and  $k$  are used for collapse in each dimension. In general it is not required that we use the same parameters, but we have done so to show how strong the agreement is between the methods used to approach jamming. Shown are  $d= 3$  (black), 4 (purple), 5 (blue), 6 (green), 7 (orange), 8 (red).

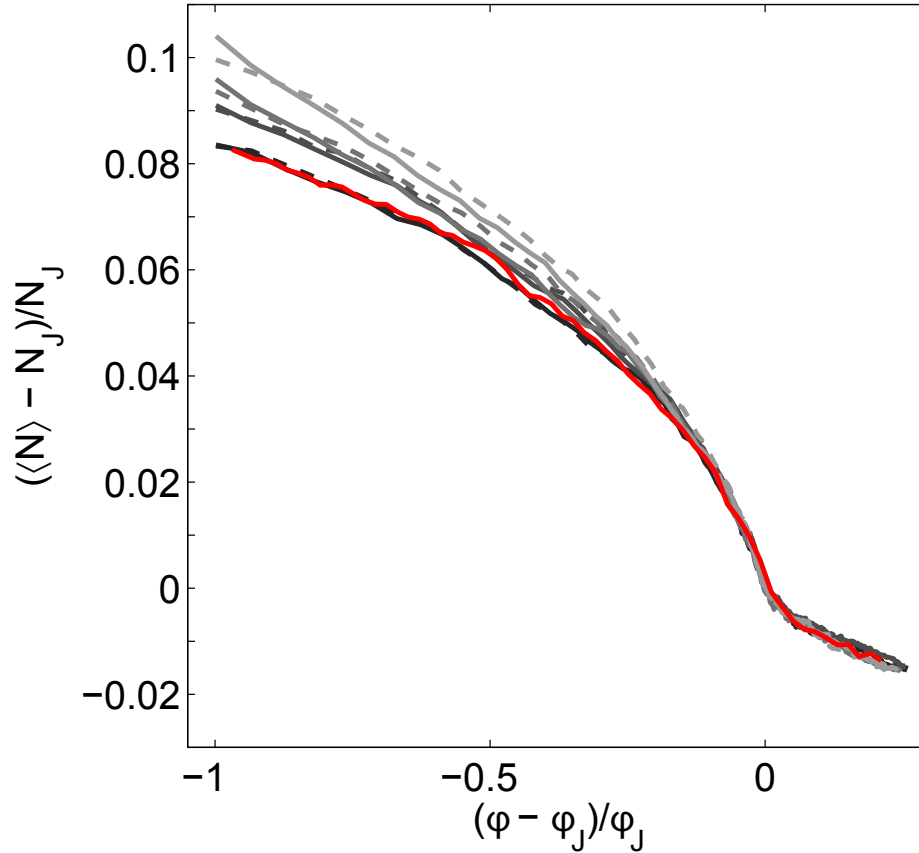


FIGURE 17. Scaled mean number of neighbors vs. scaled packing fraction for various neighbor definitions with polydisperse data in  $d = 3$ . Solid lines represent Additively Weighted Voronoi, and dashed lines represent Radical Voronoi (also called the Laguerre tessellation). Behavior at the phase transition is robust against neighbor definitions. As in Figure 2b, values of the order of the potential  $\alpha$  range from 1.5 (black) to 4 (light gray) with the Hookean potential ( $\alpha = 2$ ) shown in red.

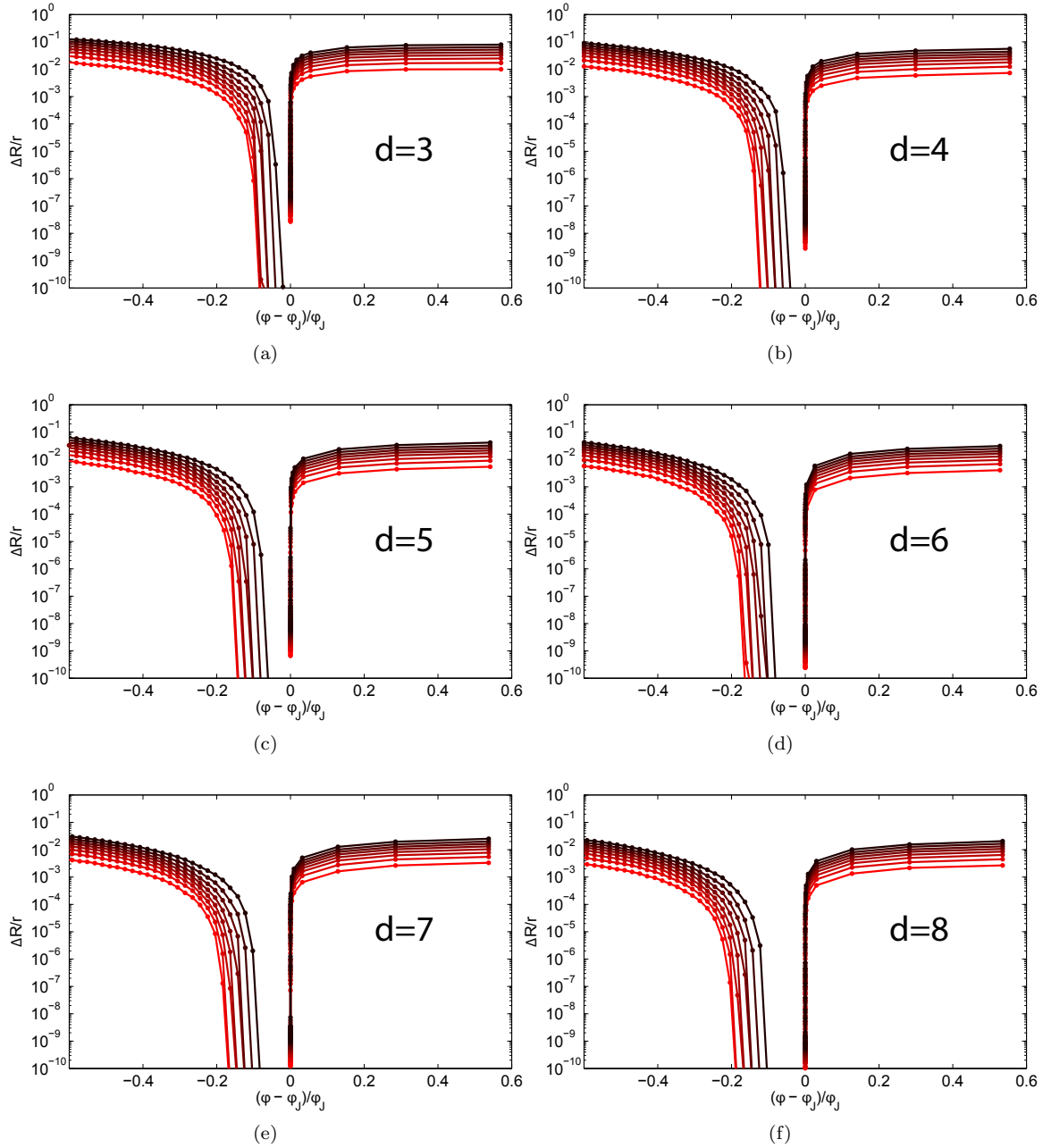


FIGURE 18. Width of the distribution of Maximum Inscribed Spheres calculated from the middle 15% (red) to 85% (black) of the distribution in steps of 10%. A width of 80% is used in the text. Note that each definition corresponds to a slightly different  $\phi^*$ , but that the general trend of  $\phi^*$  with dimension is robust. The packings analyzed are the same as seen in Figure 3b in the paper. The packings above  $\phi_J$  are made using a Geometric Mean search and the packings from below are made via Infinite Quench.

## CHAPTER VI

### SUPPLEMENTARY MATERIAL FOR CHAPTER 3

In the main manuscript, we examine the effect of dimension on the geometric order parameters associated with the Voronoi tessellation as we approach jamming. While the majority of the work is done with monodisperse spheres, in  $d = 2$  monodisperse disks spontaneously crystalize. We thus use a 50:50 mixture of bidisperse disks with a 1:1.4 ratio of radii which are known to exhibit jamming. In doing so, we observe that the scaling of the standard deviation of the volume and the internal angle differs from the  $d = 3 - 5$  case. It is not immediately clear whether this is a dimensional effect, an effect of the bidispersity, or both. In this supplement, we compare  $d = 3$  systems of 16384 particles with a 50:50 mixture of 1:1.4 ratio of radii to the monodisperse  $d = 3$  cases presented in the manuscript. We still observe power law scaling in all of the order parameters, with the possible exception of internal angle when approaching from below. However, the power laws for each parameter are not consistent with the power laws for monodisperse spheres. This seems to suggest that bidispersity and dimensional effects cannot be decoupled.

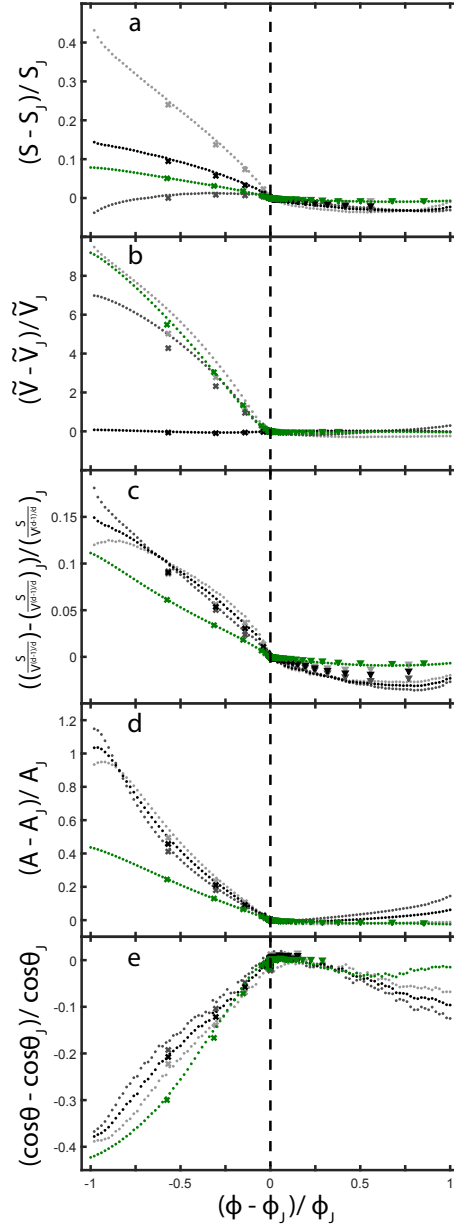


FIGURE 19. Plots of scaled order parameters vs. the scaled packing fraction. Closed circles represent IQ data, x's represent GM data (from below), and triangles represent ES data (from above). Note that on this linear scale the GM and ES data is nearly all clustered right at  $\phi_j$ . The parameters shown are (a) mean surface area,  $S$ , (b) standard deviation of volume divided by the mean of the volume,  $\tilde{V}$ , (c) mean surface to volume ratio  $S/V^{(d-1)/d}$  (d) mean aspect ratio,  $A$ , and (e) mean aspect ratio angle  $\cos\theta$ . We plot data for  $d = 3$  bidisperse spheres (smaller particles light gray, larger particles dark gray, combined black) and  $d = 3$  monodisperse spheres (green).

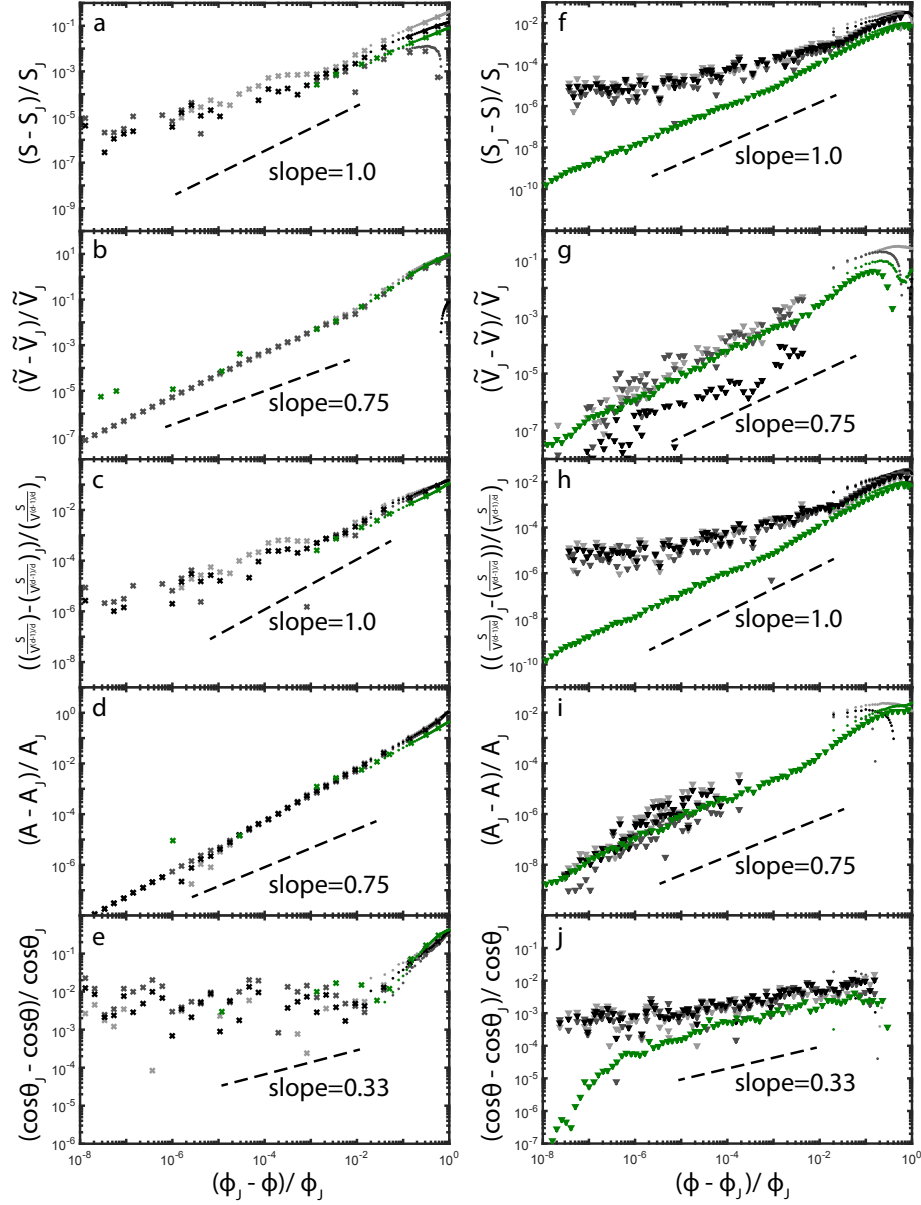


FIGURE 20. Log-log plots of each scaled order parameter vs. the scaled packing fraction approaching jamming from below (left) and above (right). Closed circles represent IQ data, x's represent GM data (from below), and triangles represent ES data (from above). The parameters shown are (a,f) mean surface area,  $S$ , (b,g) standard deviation of volume divided by the mean of the volume,  $\tilde{V}$ , (c,h) mean surface to volume ratio  $S/V^{(d-1)/d}$  (d,i) mean aspect ratio,  $A$ , and (e,j) mean aspect ratio angle  $\cos\theta$ . We plot data for  $d = 3$  bidisperse spheres (smaller particles light gray, larger particles dark gray, combined black) and  $d = 3$  monodisperse spheres (green). The slopes shown give the power laws for monodisperse spheres for comparison.

## CHAPTER VII

### CONCLUSION

This work has established that geometry plays an important role in the jamming transition. It has given a new set of tools with which to explore all of the familiar properties of a phase transition. With these new tools, there are many questions that have been answered and many more that are left for future work.

In chapter 2, I showed that there is a phase transition precisely coinciding with the jamming transition in the mean number of neighbors of a particle's Voronoi cell. This phase transition is independent of preparation protocol within the parameters tested and shows power law scaling. Most importantly, that power law shows the same behavior when approaching the transition point from above and below. This was the first indication of a transition parameter that could treat all of phase space equally.

In addition, chapter 2 introduced the concept of the maximum inscribed sphere of the Voronoi cell, which shows a different behavior when approaching the transition point from above and below. From below, there are two phase transitions: one at jamming and one significantly below jamming. This pre-jamming phase transition happens when the distribution of radii of the maximum inscribed spheres becomes a delta function. I explored this concept further in chapter 4, but the importance of this phase transition is that it gives a link between the geometry of the Voronoi cells and the underlying particles. In the phase space between the two transitions, all non-rattler particles are exactly equal to the maximum inscribed spheres of their Voronoi cells, and thus there is a constraint on the phase space. This constraint manifests itself in a new symmetry of the jamming phase space.

In chapter 3, I have shown that the phase transition explored in chapter 2 was not specific to the mean number of neighbors. Indeed all of the shape parameters that I tested (barring the maximum inscribed sphere) showed a similar phase transition at the jamming point. They all show power law behavior that is independent of packing protocol within the parameters tested. This indicates that the jamming transition is a change in the local environment of a particle, as this is what the Voronoi cell shape encodes. It is interesting to note that none of the shape parameters have a pre-jamming phase transition. It seems likely that this is because



the underlying particles don't provide any constraints on the Voronoi cell's surface area, volume, aspect ratio, or number of neighbors. Without an added constraint, I would not expect an extra transition, and so it is unsurprising that none is seen.

Furthermore, in chapter 3 I have shown that the Voronoi cell has an orientation characterized by the aspect ratio, and the correlation of cell orientations as a function of distance between particles, shows a signature of the jamming transition. This provides a natural correlation length, which may prove useful when attempting to characterize the transition from a field theory perspective.

In chapter 4, I introduced two transformations which were designed to explore hidden symmetries of the jamming transition. I defined the maximum inscribed sphere inversion as a transformation which keeps jammed systems fixed initially, and lets all other systems flow to different fixed points. The symmetry associated with this transformation is one in which jammed particles are equal to the maximum inscribed spheres of their Voronoi cells. Through this transformation, the same pre-jamming transition discussed in chapter 2 is revealed. The real space coarsening was designed to keep parameter curves fixed with respect to packing fraction. Upon coarsening, I found that the aspect ratio and the surface area retained knowledge of the underlying packing, and the curves remained fixed when using an appropriate rescaling. The hope in doing this was to flesh out the symmetries that one would find in renormalizable fields in a complete field theory. Namely, I wanted to find an order parameter which, upon coarse graining, took one value above jamming and one value below jamming, which the aspect ratio does. A field theory for the jamming transition, however, does not exist. The intent in creating this transformation was to mimic renormalization and to see whether something interesting came out of the process, and in that goal I was successful.

Because my work has taken an entirely new approach to understanding jammed systems, it has opened up a vast field of possibilities for further research. Some of these will be explored further within Eric Corwin's lab, and some will be directly applicable to the work that I will do with Lisa Manning at Syracuse University. It is quite fortunate that both are members of a recently awarded Simons' Foundation grant. The collaborative group of 13 professors who are involved will work to unify the jamming and glass transitions into a full theory. Some of the work

that I will suggest will further those aims, and other pieces will simply tie up loose ends that I find important.

The most obvious extension for most of this work is to push towards higher dimensional results. While  $d = 5$  and  $d = 8$  are plenty high for many applications, there is much that can be said if the infinite dimensional limit is known. It is in this limit that the glass transition has been exactly mapped via the replica symmetry model by Zamponi, Parisi, and Charbonneau [1]. By pushing the simulations to higher dimensions, the infinite dimensional limit can be extrapolated more effectively. However, this is futile at a certain point. The simulation time and the calculation time for all the quantities that I measure go at best exponentially and at worst factorially with dimension. If an analytic solution were found for the values of the parameters at the transition and their power laws as a function of dimension, one could take the appropriate limits and have grounds for comparison with the replica symmetry model. This work has already begun by comparing the scaling of weak contact forces in my systems with the exact infinite dimensional result [41].

Along these same lines, I think it is worth pursuing the aspect ratio of the Voronoi cell as a potentially renormalizable field with which one can create a field theory for jamming. While I have developed a coarse graining procedure which may be useful, and I have demonstrated a correlation function involving those components, there is much work to be done. First, the correlation function should be checked to see if it changes upon renormalization. This will require larger system sizes, which my analysis can easily handle. Next, it is important to find an approximate functional form that shows how the aspect ratio changes upon coarse graining. If a form were found, the appropriate limits could be taken to see how the arbitrarily large systems behave. It will then be important to find a functional which is analogous to an energy which will be minimized. This is not a trivial task, but it is the key in transforming my work into a field theory.

Another direction that should be taken with this work is the application to hard sphere glasses in finite dimensions. It is trivial to calculate all of the geometric quantities that I have described at any snapshot of a thermal system. However, this hardly captures the complexity that a hard sphere glass exhibits. It would be helpful to develop the algorithms to calculate first order fluctuations in the geometric properties of the Voronoi cells with small movements of particles. It

would then be useful to analyze systems where temperature is a small parameter so that one could perhaps find interesting relations between temperature and the average distribution width of each parameter.

A new direction that I have begun to probe is the phase space relations between soft spheres and hard spheres, as they share the same configuration space below and at jamming. One trajectory is to map out the local phase space environment of a system. With a phase space dimensionality of  $N * d$  (where  $N$  is the number of particles and  $d$  is the dimension) this is no easy task. There are two manageable paths to take. One is to take a step in a random phase space directions, which will in general always correspond to a higher energy. The energy can then be reminimized to see if the system ends up in the same phase space configuration or whether it relaxes into a new configuration. Repeating this process for different step sizes will give the average well depth. It could also indicate whether the phase space is fractal, which will be instrumental in determining whether there is a Gardner transition before or at jamming [58]. The other useful approach is to choose an eigendirection in phase space, which correspond to global soft modes. Mapping out the length of the allowable steps in these eigendirections will again give access to the fractality of the phase space.

There are other applications of this work in cell networks, which is what I will be exploring in my post doctoral position at Syracuse. Specifically, there is a glass transition in two dimensional biological cells that can be well explained by the self-propelled Voronoi (SPV) model. The SPV model correctly predicts that the glass transition happens when the dimensionless surface to volume ratio of the cells reaches a value of 3.81 [62], which is consistent with the value I have measured for bidisperse particles at jamming [9]. I am currently collaborating with the Manning group to see if the aspect ratio and the standard deviation of the volume also match up between the two transitions. Their group is also investigating three dimensional cells using the same model, and preliminary data shows that the dimensionless surface to volume ratio matches between the two transitions. My first task at Syracuse will be to investigate whether there is any theoretical basis for the lining up of these two transitions.

Finally, I would like to investigate the application of this work to experimental systems. As with simulations, there are two avenues to consider: hard spheres and soft colloids. Soft colloids are advantageous in that there are a wide range of packing fractions available above and below

jamming [63], but spheres above jamming can have significant deformations which may make the application of my results less concrete. Hard sphere systems present their own problems, as they are only available below the phase transition. And while simulations can provide arbitrary precision, power law scaling in experiments will be difficult to confirm, as the precision in particle centers and radii is always quite limited [63]. It would be beneficial for my lab to seek out experimentalists to share data with, as many of these experiments require great expertise. In my lab, we once had a summer project led by Ben Strickland who attempted to use sedimenting spheres in a suspension to obtain a variety of packing fractions as a function of height. However, the difficulties in obtaining high precision results should not be a deterrent to this line of work. The notion that the physics governing this transition depends on highly tuned experimental parameters seems fundamentally flawed. If it were true, then the exercise that you began with, a walk on the beach, could have wildly varying and unfortunate consequences depending on where you stepped.

## REFERENCES CITED

- [1] Giorgio Parisi and Francesco Zamponi. Mean-field theory of hard sphere glasses and jamming. *Reviews of Modern Physics*, 82(1):789–845, March 2010. doi: 10.1103/RevModPhys.82.789. URL <http://link.aps.org/doi/10.1103/RevModPhys.82.789>.
- [2] Chaoming Song, Ping Wang, and Hernn A. Makse. A phase diagram for jammed matter. *Nature*, 453(7195):629–632, May 2008. ISSN 0028-0836. doi: 10.1038/nature06981. URL <http://www.nature.com/nature/journal/v453/n7195/full/nature06981.html>.
- [3] Leonardo E. Silbert, Deniz Ertar, Gary S. Grest, Thomas C. Halsey, and Dov Levine. Geometry of frictionless and frictional sphere packings. *Physical Review E*, 65(3):031304, February 2002. doi: 10.1103/PhysRevE.65.031304. URL <http://link.aps.org/doi/10.1103/PhysRevE.65.031304>.
- [4] S. Henkes, M. van Hecke, and W. van Saarloos. Critical jamming of frictional grains in the generalized isostaticity picture. *EPL (Europhysics Letters)*, 90(1):14003, 2010. ISSN 0295-5075. doi: 10.1209/0295-5075/90/14003. URL <http://stacks.iop.org/0295-5075/90/i=1/a=14003>.
- [5] Stefanos Papanikolaou, Corey S. O'Hern, and Mark D. Shattuck. Isostaticity at Frictional Jamming. *Physical Review Letters*, 110(19):198002, May 2013. doi: 10.1103/PhysRevLett.110.198002. URL <http://link.aps.org/doi/10.1103/PhysRevLett.110.198002>.
- [6] Corey S. O'Hern, Leonardo E. Silbert, Andrea J. Liu, and Sidney R. Nagel. Jamming at zero temperature and zero applied stress: The epitome of disorder. *Physical Review E*, 68(1):011306, July 2003. doi: 10.1103/PhysRevE.68.011306. URL <http://link.aps.org/doi/10.1103/PhysRevE.68.011306>.
- [7] Georges Voronoi. Nouvelles applications des paramtres continus la thorie des formes quadratiques. Deuxime mmoire. Recherches sur les paralllloedres primitifs. : Journal fr die reine und angewandte Mathematik (Crelle's Journal). *Journal Fur Die Reine Und Angewandte Mathematik*, pages 198–287, 1908. URL <http://www.degruyter.com/view/j/crll.1908.issue-134/crll.1908.134.198/crll.1908.134.198.xml>.
- [8] Peter K. Morse and Eric I. Corwin. Geometric Signatures of Jamming in the Mechanical Vacuum. *Physical Review Letters*, 112(11):115701, March 2014. doi: 10.1103/PhysRevLett.112.115701. URL <http://link.aps.org/doi/10.1103/PhysRevLett.112.115701>.
- [9] Peter K. Morse and Eric I. Corwin. Geometric order parameters derived from the Voronoi tessellation show signatures of the jamming transition. *Soft Matter*, 12(4):1248–1255, January 2016. ISSN 1744-6848. doi: 10.1039/C5SM02575C. URL <http://pubs.rsc.org/en/content/articlelanding/2016/sm/c5sm02575c>.
- [10] S. Hales. Vegetable staticks. *W. and J. Innys and T. Woodward, London, UK*, 1727.
- [11] M. Wyart. On the rigidity of amorphous solids. *Annales de Physique*, 30(3):1–96, 2005. ISSN 0003-4169, 1286-4838. doi: 10.1051/anphys:2006003.
- [12] Wouter G. Ellenbroek, Ellk Somfai, Martin van Hecke, and Wim van Saarloos. Critical Scaling in Linear Response of Frictionless Granular Packings near Jamming. *Physical Review Letters*, 97(25):258001, December 2006. doi: 10.1103/PhysRevLett.97.258001. URL <http://link.aps.org/doi/10.1103/PhysRevLett.97.258001>.

- [13] Brian P. Tighe, Erik Woldhuis, Joris J. C. Remmers, Wim van Saarloos, and Martin van Hecke. Model for the Scaling of Stresses and Fluctuations in Flows near Jamming. *Physical Review Letters*, 105(8):088303, 2010. doi: 10.1103/PhysRevLett.105.088303. URL <http://link.aps.org/doi/10.1103/PhysRevLett.105.088303>.
- [14] Corey S. O'Hern, Stephen A. Langer, Andrea J. Liu, and Sidney R. Nagel. Force Distributions near Jamming and Glass Transitions. *Physical Review Letters*, 86(1):111–114, January 2001. doi: 10.1103/PhysRevLett.86.111. URL <http://link.aps.org/doi/10.1103/PhysRevLett.86.111>.
- [15] Corey S. O'Hern, Stephen A. Langer, Andrea J. Liu, and Sidney R. Nagel. Random Packings of Frictionless Particles. *Physical Review Letters*, 88(7):075507, January 2002. doi: 10.1103/PhysRevLett.88.075507. URL <http://link.aps.org/doi/10.1103/PhysRevLett.88.075507>.
- [16] Brian P. Tighe. Dynamic Critical Response in Damped Random Spring Networks. *Physical Review Letters*, 109(16):168303, October 2012. doi: 10.1103/PhysRevLett.109.168303. URL <http://link.aps.org/doi/10.1103/PhysRevLett.109.168303>.
- [17] M. van Hecke. Jamming of soft particles: geometry, mechanics, scaling and isostaticity. *Journal of Physics: Condensed Matter*, 22(3):033101, January 2010. ISSN 0953-8984. doi: 10.1088/0953-8984/22/3/033101. URL <http://iopscience.iop.org/0953-8984/22/3/033101>.
- [18] Monica Skoge, Aleksandar Donev, Frank H. Stillinger, and Salvatore Torquato. Packing hyperspheres in high-dimensional Euclidean spaces. *Physical Review E*, 74(4):041127, October 2006. doi: 10.1103/PhysRevE.74.041127. URL <http://link.aps.org/doi/10.1103/PhysRevE.74.041127>.
- [19] Z. W. Salsburg and W. W. Wood. Equation of State of Classical Hard Spheres at High Density. *The Journal of Chemical Physics*, 37(4):798–804, 1962. ISSN 0021-9606, 1089-7690. doi: 10.1063/1.1733163. URL <http://scitation.aip.org/content/aip/journal/jcp/37/4/10.1063/1.1733163>.
- [20] Aleksandar Donev, Frank H. Stillinger, and Salvatore Torquato. Unexpected Density Fluctuations in Jammed Disordered Sphere Packings. *Physical Review Letters*, 95(9):090604, 2005. doi: 10.1103/PhysRevLett.95.090604. URL <http://link.aps.org/doi/10.1103/PhysRevLett.95.090604>.
- [21] Walter Kob and Ludovic Berthier. Probing a Liquid to Glass Transition in Equilibrium. *Physical Review Letters*, 110(24):245702, June 2013. doi: 10.1103/PhysRevLett.110.245702. URL <http://link.aps.org/doi/10.1103/PhysRevLett.110.245702>.
- [22] Patrick Charbonneau, Atsushi Ikeda, Giorgio Parisi, and Francesco Zamponi. Glass Transition and Random Close Packing above Three Dimensions. *Physical Review Letters*, 107(18):185702, October 2011. doi: 10.1103/PhysRevLett.107.185702. URL <http://link.aps.org/doi/10.1103/PhysRevLett.107.185702>.
- [23] Patrick Charbonneau, Eric I. Corwin, Giorgio Parisi, and Francesco Zamponi. Universal Microstructure and Mechanical Stability of Jammed Packings. *Physical Review Letters*, 109(20):205501, November 2012. doi: 10.1103/PhysRevLett.109.205501. URL <http://link.aps.org/doi/10.1103/PhysRevLett.109.205501>.
- [24] Carl P. Goodrich, Andrea J. Liu, and Sidney R. Nagel. Finite-Size Scaling at the Jamming Transition. *arXiv:1204.4915*, April 2012. URL <http://arxiv.org/abs/1204.4915>.

- [25] J. A. Dodds. Simplest statistical geometric model of the simplest version of the multicomponent random packing problem. *Nature*, 256(5514):187–189, July 1975. ISSN  $\{\text{footerJournalISSN}\}$ . doi: 10.1038/256187a0. URL <http://www.nature.com/nature/journal/v256/n5514/abs/256187a0.html>.
- [26] Maxime Clusel, Eric I. Corwin, Alexander O. N. Siemens, and Jasna Bruji. A granocentric model for random packing of jammed emulsions. *Nature*, 460(7255):611–615, July 2009. ISSN 0028-0836. doi: 10.1038/nature08158. URL <http://www.nature.com/nature/journal/v460/n7255/full/nature08158.html>.
- [27] James G. Puckett, Frdric Lechenault, and Karen E. Daniels. Local origins of volume fraction fluctuations in dense granular materials. *Physical Review E*, 83(4):041301, April 2011. doi: 10.1103/PhysRevE.83.041301. URL <http://link.aps.org/doi/10.1103/PhysRevE.83.041301>.
- [28] Katherine A. Newhall, Ivane Jorjadze, Eric Vanden-Eijnden, and Jasna Brujic. A statistical mechanics framework captures the packing of monodisperse particles. *Soft Matter*, 7(24):11518, 2011. ISSN 1744-683X, 1744-6848. doi: 10.1039/c1sm06243c. URL <http://pubs.rsc.org/en/Content/ArticleLanding/2011/SM/c1sm06243c>.
- [29] C. B. O’Donovan, E. I. Corwin, and M. E. Mbius. Mean-field granocentric approach in 2d & 3d polydisperse, frictionless packings. arXiv e-print 1302.2511, February 2013. URL <http://arxiv.org/abs/1302.2511>.
- [30] Franco P. Preparata and Michael Ian Shamos. *Computational geometry: an introduction*. Springer-Verlag, 1985.
- [31] Eric I. Corwin, Robin Stinchcombe, and M. F. Thorpe. Bond percolation in higher dimensions. *Physical Review E*, 88(1):014102, July 2013. doi: 10.1103/PhysRevE.88.014102. URL <http://link.aps.org/doi/10.1103/PhysRevE.88.014102>.
- [32] Magnus R Hestenes and Eduard Stiefel. Methods of Conjugate Gradients for Solving Linear Systems1. *Journal of Research of the National Bureau of Standards*, 49(6), 1952.
- [33] Erik Bitzek, Pekka Koskinen, Franz Ghler, Michael Moseler, and Peter Gumbsch. Structural Relaxation Made Simple. *Physical Review Letters*, 97(17):170201, October 2006. doi: 10.1103/PhysRevLett.97.170201. URL <http://link.aps.org/doi/10.1103/PhysRevLett.97.170201>.
- [34] V Privman, PC Hohenberg, and A Aharony. *Phase Transitions and Critical Phenomena*, volume 14. Academic, New York, 1991.
- [35] J. L. Meijering. Interface area, edge length, and number of vertices in crystal aggregates with random nucleation. *Philips Res. Rep*, 8(1953):270–290, 1953.
- [36] J. Mller. Random Tessellations in Rd. *Advances in Applied Probability*, 21(1):37–73, March 1989. ISSN 0001-8678. doi: 10.2307/1427197.
- [37] Robert S. Farr and Robert D. Groot. Close packing density of polydisperse hard spheres. *The Journal of Chemical Physics*, 131(24):244104–244104–7, December 2009. ISSN 00219606. doi: doi:10.1063/1.3276799.
- [38] Andrea J. Liu and Sidney R. Nagel. Nonlinear dynamics: Jamming is not just cool any more. *Nature*, 396(6706):21–22, November 1998. ISSN 0028-0836. doi: 10.1038/23819. URL <http://www.nature.com/nature/journal/v396/n6706/full/396021a0.html>.

- [39] Romain Mari, Florent Krzakala, and Jorge Kurchan. Jamming versus Glass Transitions. *Physical Review Letters*, 103(2):025701, July 2009. doi: 10.1103/PhysRevLett.103.025701. URL <http://link.aps.org/doi/10.1103/PhysRevLett.103.025701>.
- [40] Dapeng Bi, Jie Zhang, Bulbul Chakraborty, and R. P. Behringer. Jamming by shear. *Nature*, 480(7377):355–358, December 2011. ISSN 0028-0836. doi: 10.1038/nature10667. URL <http://www.nature.com/nature/journal/v480/n7377/full/nature10667.html>.
- [41] Patrick Charbonneau, Eric I. Corwin, Giorgio Parisi, and Francesco Zamponi. Jamming Criticality Revealed by Removing Localized Buckling Excitations. *Physical Review Letters*, 114(12):125504, March 2015. doi: 10.1103/PhysRevLett.114.125504. URL <http://link.aps.org/doi/10.1103/PhysRevLett.114.125504>.
- [42] Stephen Whitelam, Ludovic Berthier, and Juan P. Garrahan. Dynamic Criticality in Glass-Forming Liquids. *Physical Review Letters*, 92(18):185705, May 2004. doi: 10.1103/PhysRevLett.92.185705. URL <http://link.aps.org/doi/10.1103/PhysRevLett.92.185705>.
- [43] J. D. Bernal and J. L. Finney. Random close-packed hard-sphere model. II. Geometry of random packing of hard spheres. *Discussions of the Faraday Society*, 43(0):62–69, January 1967. ISSN 0366-9033. doi: 10.1039/DF9674300062. URL <http://pubs.rsc.org/en/content/articlelanding/1967/df/df9674300062>.
- [44] Keishi Gotoh and John L. Finney. Statistical geometrical approach to random packing density of equal spheres. *Nature*, 252(5480):202–205, November 1974. doi: 10.1038/252202a0. URL <http://www.nature.com/nature/journal/v252/n5480/abs/252202a0.html>.
- [45] Steven Slotterback, Masahiro Toiya, Leonard Goff, Jack F. Douglas, and Wolfgang Losert. Correlation between Particle Motion and Voronoi-Cell-Shape Fluctuations during the Compaction of Granular Matter. *Physical Review Letters*, 101(25):258001, December 2008. doi: 10.1103/PhysRevLett.101.258001. URL <http://link.aps.org/doi/10.1103/PhysRevLett.101.258001>.
- [46] Eric I. Corwin, Maxime Clusel, Alexander O. N. Siemens, and Jasna Bruji. Model for random packing of polydisperse frictionless spheres. *Soft Matter*, 6(13):2949, 2010. ISSN 1744-683X, 1744-6848. doi: 10.1039/c000984a. URL <http://pubs.rsc.org/en/Content/ArticleLanding/2010/SM/c000984a>.
- [47] Jean-Daniel Boissonnat and Christophe Delage. Convex Hull and Voronoi Diagram of Additively Weighted Points. In *Algorithms ESA 2005*, volume 3669, pages 367–378. Springer Berlin Heidelberg, Berlin, Heidelberg, 2005. ISBN 978-3-540-29118-3 978-3-540-31951-1.
- [48] B Delaunay. Sur la sphre vide. A la mmoire de Georges Vorono. *Bulletin de l'Acadmie des Sciences de l'URSS. Classe des sciences mathmatiques et na*, (6):793–800, 1934.
- [49] Jesper Mller. Random Johnson-Mehl Tessellations. *Advances in Applied Probability*, 24(4): 814–844, December 1992. ISSN 0001-8678. doi: 10.2307/1427714.
- [50] Eloi Pineda, Victor Garrido, and Daniel Crespo. Domain-size distribution in a Poisson-Voronoi nucleation and growth transformation. *Physical Review E*, 75(4):040107, April 2007. doi: 10.1103/PhysRevE.75.040107. URL <http://link.aps.org/doi/10.1103/PhysRevE.75.040107>.



- [51] Jordi Farjas and Pere Roura. Cell size distribution in a random tessellation of space governed by the Kolmogorov-Johnson-Mehl-Avrami model: Grain size distribution in crystallization. *Physical Review B*, 78(14):144101, October 2008. doi: 10.1103/PhysRevB.78.144101. URL <http://link.aps.org/doi/10.1103/PhysRevB.78.144101>.
- [52] Abraham. Savitzky and M. J. E. Golay. Smoothing and Differentiation of Data by Simplified Least Squares Procedures. *Analytical Chemistry*, 36(8):1627–1639, July 1964. ISSN 0003-2700. doi: 10.1021/ac60214a047. URL <http://dx.doi.org/10.1021/ac60214a047>.
- [53] J. D. Bernal, J. Mason, and K. R. Knight. Radial Distribution of the Random Close Packing of Equal Spheres. *Nature*, 194(4832):957–958, June 1962. doi: 10.1038/194957a0. URL <http://www.nature.com/nature/journal/v194/n4832/abs/194957a0.html>.
- [54] Aleksandar Donev, Salvatore Torquato, and Frank H. Stillinger. Pair correlation function characteristics of nearly jammed disordered and ordered hard-sphere packings. *Physical Review E*, 71(1):011105, January 2005. doi: 10.1103/PhysRevE.71.011105. URL <http://link.aps.org/doi/10.1103/PhysRevE.71.011105>.
- [55] J. Clerk Maxwell. On the calculation of the equilibrium and stiffness of frames. *Philosophical Magazine Series 4*, 27(182):294–299, April 1864. ISSN 1941-5982. doi: 10.1080/14786446408643668. URL <http://www.tandfonline.com/doi/abs/10.1080/14786446408643668>.
- [56] Remi Dreyfus, Ye Xu, Tim Still, L. A. Hough, A. G. Yodh, and Salvatore Torquato. Diagnosing hyperuniformity in two-dimensional, disordered, jammed packings of soft spheres. *Physical Review E*, 91(1):012302, January 2015. doi: 10.1103/PhysRevE.91.012302. URL <http://link.aps.org/doi/10.1103/PhysRevE.91.012302>.
- [57] Moumita Maiti and Srikanth Sastry. Free volume distribution of nearly jammed hard sphere packings. *The Journal of Chemical Physics*, 141(4):044510, July 2014. ISSN 0021-9606, 1089-7690. doi: 10.1063/1.4891358. URL <http://scitation.aip.org/content/aip/journal/jcp/141/4/10.1063/1.4891358>.
- [58] Patrick Charbonneau, Jorge Kurchan, Giorgio Parisi, Pierfrancesco Urbani, and Francesco Zamponi. Fractal free energy landscapes in structural glasses. *Nature Communications*, 5, April 2014. doi: 10.1038/ncomms4725. URL <http://www.nature.com/ncomms/2014/140424/ncomms4725/full/ncomms4725.html>.
- [59] Stephen Boyd and Lieven Vandenberghe. *Convex Optimization*. Cambridge University Press, March 2004. ISBN 978-1-107-39400-1.
- [60] George Y. Onoda and Eric G. Liniger. Random loose packings of uniform spheres and the dilatancy onset. *Physical Review Letters*, 64(22):2727–2730, May 1990. doi: 10.1103/PhysRevLett.64.2727. URL <http://link.aps.org/doi/10.1103/PhysRevLett.64.2727>.
- [61] Giorgio Parisi and Francesco Zamponi. The ideal glass transition of hard spheres. *The Journal of Chemical Physics*, 123(14):144501–144501–12, October 2005. ISSN 00219606. doi: doi:10.1063/1.2041507.
- [62] Dapeng Bi, Xingbo Yang, M. Cristina Marchetti, and M. Lisa Manning. Motility-driven glass and jamming transitions in biological tissues. *arXiv:1509.06578 [cond-mat, physics:physics]*, September 2015. URL <http://arxiv.org/abs/1509.06578>. arXiv: 1509.06578.

- [63] Wilson C. K. Poon, Eric R. Weeks, and C. Patrick Royall. On measuring colloidal volume fractions. *Soft Matter*, 8(1):21–30, December 2011. ISSN 1744-6848. doi: 10.1039/C1SM06083J. URL <http://pubs.rsc.org/en/content/articlelanding/2012/sm/c1sm06083j>.